Nature Communications

https://doi.org/10.1038/s41467-026-75031-7

Article in Press

ZNF689 loss impairs homologous recombination sensitizing triple-negative breast cancer to combined PARP and PD-L1 inhibition

Received: 5 February 2025

Accepted: 15 June 2026

Published online: 04 July 2026

Cite this article as: Ge, L.-P., Xiao, Y.-L., Wu, S.-Y. *et al.* ZNF689 loss impairs homologous recombination sensitizing triple-negative breast cancer to combined PARP and PD-L1 inhibition. *Nat Commun* (2026). https://doi.org/10.1038/s41467-026-75031-7

Li-Ping Ge, Yu-Ling Xiao, Song-Yang Wu, Fang-Lin Zhang, Eo-Ryeong Lee, Gen-Hong Di, Zhi-Ming Shao, Minhong Shen & Yi-Zhou Jiang

ZNF689 loss impairs homologous recombination sensitizing triple-negative breast cancer to combined PARP and PD-L1 inhibition

Author list:

Li-Ping Ge (葛丽萍)[1,2†], Yu-Ling Xiao (肖玉铃)[1,2†], Song-Yang Wu (吴松阳)[1,2†], Fang-Lin Zhang (张方淋)[1,2], Eo-Ryeong Lee (李於昤)[1,2], Gen-Hong Di (狄根红)[1,2], Zhi-Ming Shao (邵志敏)[1,2], Minhong Shen (沈敏洪)[1,2], Yi-Zhou Jiang (江一舟)[1,2,3*]

Affiliations:

1 Key Laboratory of Breast Cancer in Shanghai, Department of Breast Surgery, Precision Cancer Medicine Center, Fudan University Shanghai Cancer Center, Shanghai 200032, P. R. China.

2 Department of Oncology, Shanghai Medical College, Fudan University, Shanghai 200032, P. R. China.

3 Shanghai Academy of Natural Sciences (SANS), Fudan University, Shanghai 200032, P. R. China.

† These authors contributed equally: Li-Ping Ge, Yu-Ling Xiao, Song-Yang Wu

***Correspondence:** Dr. Yi-Zhou Jiang, yizhoujiang@fudan.edu.cn

Abstract

Triple-negative breast cancer (TNBC) is the most aggressive subtype of breast cancer, characterized by a poor prognosis due to the lack of effective targeted therapies. While poly (ADP-ribose) polymerase (PARP) inhibitors benefit BRCA1/2-mutated TNBC, their efficacy in BRCA wild-type tumors remains limited. In this study, we uncover a critical role of zinc finger protein 689 (ZNF689) in regulating homologous recombination (HR) repair in TNBC. Our findings reveal that ZNF689, upon phosphorylation by ATM, promotes NBS1 ubiquitination via E3 ligase SKP2, leading to the stabilization of the MRN complex and subsequent ATM activation, thereby facilitating HR repair. ZNF689 loss markedly enhances sensitivity to PARP inhibitors in TNBC, particularly when combined with paclitaxel. Furthermore, PARP inhibitor upregulates PD-L1 expression in ZNF689-deficient TNBC cells through activation of the STING pathway. Notably, ZNF689 loss enhances the therapeutic efficacy of PARP inhibitor plus anti-PD-L1 immunotherapy. Together, these findings suggest ZNF689 as a crucial regulator of HR repair and provide proof-of-concept for combining PARP inhibition and PD-L1 blockade in patients with ZNF689-low TNBC.

Introduction

Triple-negative breast cancer (TNBC) is a heterogeneous and highly aggressive subtype of breast cancer, associated with poor overall survival and a high risk of distant recurrence[1]. Traditional chemotherapy has limited efficacy in TNBC[2]. A subset of TNBCs is BRCA-associated and deficient in homologous recombination (HR) repair[3]. The inhibition of poly (ADP-ribose) polymerase (PARP) in HR-deficient (HRD) tumors has demonstrated synthetic lethality through diverse mechanisms, including the catalytic inhibition of PARP enzymes and the entrapment of PARP-DNA complexes[4]. Consequently, agents such as olaparib and talazoparib have exhibited improved efficacy specifically in BRCA-associated breast cancers, when compared to standard chemotherapy[5-7]. However, these benefits are limited in BRCA wild-type (WT) cancers, which are more prevalent in clinical practice. Therefore, identifying biomarkers for PARP inhibitor (PARPi) response beyond BRCA status, as well as exploring effective combination strategies with PARPi, are crucial for enhancing treatment efficacy in TNBC.

The generation of DNA double-strand breaks (DSBs) seriously threatens genomic stability and cellular viability. To safeguard the accurate transmission of genetic information, cells activate a DNA damage response (DDR) upon DSB induction. This response entails the activation of kinases such as ATM, ATR, and DNA-PKcs, which subsequently phosphorylate downstream substrates[8]. These events trigger a cascade of molecular events that include cell cycle arrest, post-translational modification and transcriptional regulation of repair-related proteins, and recruitment of repair proteins to the sites with damage[9,10]. Two main strategies have evolved to

repair DSBs: non-homologous end-joining (NHEJ) and HR[11]. NHEJ directly joins broken DNA ends but can cause mutations[12], while HR is an error-free repair mechanism using a homologous template[13]. Clinically, the integrity of the HR repair pathway is used to predict patient responsiveness to PARPi[14]. Therefore, identifying additional regulators of HR repair could broaden the application of PARPi in treating TNBC, ultimately enhancing patient outcomes.

Zinc finger proteins (ZNFs) are among the most abundant transcription factor families in the human genome and are involved in transcriptional regulation, chromatin remodeling, and genome stability[15]. While traditionally linked to gene expression control, emerging evidence suggests that some ZNFs also contribute to the DDR, either by regulating DNA repair gene expression or interacting with DNA repair complexes[16]. ZNF689 is a nuclear C2H2-type KRAB-ZNF family member[17], previously implicated in transcriptional regulation and cell cycle control in various cancers[17-19]. In our prior study, we identified ZNF689 as a key suppressor of intratumor heterogeneity in TNBC, acting through TRIM28-mediated silencing of long interspersed nuclear element 1 (LINE-1) retrotransposons via H3K9me3[20]. ZNF689 deficiency led to LINE-1 reactivation and increased genomic instability[20]. These findings prompted us to hypothesize that ZNF689 may play a broader role in genome maintenance, including in DSB repair. However, its involvement in DSB repair remains unknown.

In this study, we show that ZNF689 is recruited to DNA DSB sites via ATM-mediated phosphorylation in TNBC. It stabilizes the MRN complex and activates ATM through NBS1 ubiquitination during HR repair. Additionally, PARP inhibition significantly upregulates PD-L1

expression in ZNF689-deficient TNBC cells via the STING pathway. Notably, ZNF689 loss enhances the efficacy of combined PARPi and anti-PD-L1 in TNBC.

Results

ZNF689 loss impairs HR repair activity in TNBC.

To investigate the downstream pathways regulated by ZNF689 in TNBC, RNA sequencing (RNA-seq) analysis was conducted in MDA-MB-231 cells. Gene set enrichment analysis (GSEA) revealed significant enrichment of pathways related to DNA damage sites, homologous recombination, and DNA repair pathways in ZNF689-silenced cells (**Fig. 1a; Supplementary Fig. 1a and Supplementary Table 1**). Given that ZNF689 is a nuclear protein and harbors zinc finger DNA binding motif[17], we reasoned that it might play a role in these important processes. To further explore this, we assessed γH2AX level—a widely used marker of DNA damage marked by Ser139 phosphorylation[21]—at 0, 0.5, 3, 6, 12, and 24 h after ionizing radiation (IR)[22-24]. In MDA-MB-231 and BT-549 cells transfected with control siRNA, γH2AX levels peaked at early time points and progressively declined to baseline by 24 h, reflecting efficient activation and resolution of the DDR. In contrast, ZNF689-silenced cells exhibited sustained γH2AX signals during the later stages, indicative of delayed DNA repair (**Fig. 1b and c**). Specifically, while the initial γH2AX induction during the peak signaling phase (4 h post-IR) remained comparable between the groups, a pronounced retention of γH2AX emerged in ZNF689-deficient cells during the repair resolution phase (≥ 6 h post-IR) (**Supplementary Fig. 1b**). The chosen time course encompasses early sensing, active repair, and resolution phases, thus enabling a comprehensive assessment of DDR dynamics[22-26]. These findings suggest that ZNF689 is involved in the regulation of DDR and possibly the repair of DNA damage.

DNA DSBs are mainly repaired by HR and NHEJ repair pathways[27]. To assess the effect of ZNF689 on these pathways, we employed reporter systems to measure HR and NHEJ activity. The HR reporter substrate (pDR-GFP) used the GFP gene, which was interrupted by an I-SceI site. The functional GFP can only be restored by HR repair using the downstream iGFP sequence as the template after I-SceI expression[28] (**Fig. 1d**). Using U2OS, MDA-MB-231 and BT-549 DR-GFP cells, which harboring chromosomally integrated single-copy of the DR-GFP construct, the percentage of GFP-positive cells was significantly reduced in cells treated with siRNA against ZNF689 after exogenous expression of I-SceI, indicating a suppression of HR repair pathway after ZNF689 loss (**Fig. 1e and f; Supplementary Fig. 1c-e**). Furthermore, we utilized an NHEJ reporter system (EJ5-GFP), which consists of a puro gene inserted into an I-SceI site located between the promoter and the open reading frame of GFP. GFP expression can only occur through NHEJ repair pathway after the puro gene is excised by exogenous I-SceI expression[29] (**Supplementary Fig. 1f**). However, in contrast to the results of the HR reporter assay, knockdown of ZNF689 in U2OS, MDA-MB-231, and BT-549 cells stably transfected with the EJ5-GFP plasmid did not result in any significant change in GFP-positive rates (**Supplementary Fig. 1g and h**). These results suggest that ZNF689 mainly affects HR, but not NHEJ repair pathway after DNA damage in TNBC.

HR repair is initiated by loading RAD51 onto the resected single-strand DNA (ssDNA), and RAD51 foci formation is considered a marker of HR repair[30]. Consistent with the HR reporter assay, ZNF689 knockdown in MDA-MB-231 cells resulted in a significant reduction in RAD51

foci formation (**Fig. 1g**). Moreover, ectopic BRCA2 expression failed to restore RAD51 foci in ZNF689-depleted cells, suggesting that ZNF689 promotes HR repair through a BRCA2-independent mechanism (**Fig. 1g; Supplementary Fig. 1i and j**). We also observed no significant change in the formation of 53BP1 foci, a common indicator of activated NHEJ repair pathway[31], in MDA-MB-231 cells treated with siRNA against ZNF689 after the exposure to IR (**Supplementary Fig. 1k**). Furthermore, ZNF689 depletion increased IR-induced chromosomal aberrations, including chromosome breaks, rings, and arm losses, as determined by metaphase spread analysis (**Fig. 1h**). In addition, we observed no significant changes in cell cycle progression after ZNF689 knockdown (**Supplementary Fig. 1l**). Collectively, our findings suggest that ZNF689 loss impairs HR repair activity in TNBC.

Recruitment of ZNF689 to the DSBs sites depends on the Ser215 phosphorylation by ATM. Next, we tested whether ZNF689 localized to DNA damage sites to support HR repair. Proximity ligation assays (PLA) detected ZNF689–γH2AX colocalization in the nucleus after IR (**Fig. 2a**), and immunofluorescence (IF) confirmed this colocalization (**Supplementary Fig. 2a and b**). To assess the role of ZNF689 in MRN complex recruitment to DNA damage sites, we performed chromatin immunoprecipitation (ChIP) assays targeting MRE11, RAD50, and NBS1 in U2OS DR-GFP cells. After the induction of DNA DSBs by I-SceI, DNA fragments associated with these proteins were readily detected in control cells but were markedly reduced in ZNF689-depleted cells (**Fig. 2b**). These results indicate that ZNF689 is required for efficient recruitment of the

MRN complex to sites of DNA damage. Electrophoretic mobility shift assays (EMSA) demonstrated that ZNF689 is capable of binding to double-stranded DNA (dsDNA) (**Supplementary Fig. 2c-e**), which is consistent with its structural features as a zinc finger-containing transcription factor. Furthermore, competition assays with unlabeled DNA supported this general dsDNA-binding activity.

The detection of DNA damage is orchestrated by upstream kinases such as ATM, ATR, and DNA-PKcs, which phosphorylate their substrates that contain conserved serine/threonine-glutamine (S/TQ) motifs[32]. An antibody against p-S/TQ was utilized to test whether ZNF689 could be directly phosphorylated at S/TQ motif after DNA damage. We found that ZNF689 was phosphorylated at S/TQ site in response to IR treatment (**Fig. 2c**). Notably, four SQ motifs, including S215, S221, S355, and S494, are present in the human ZNF689 and conserved across species (**Fig. 2d**). We thus generated S215A, S221A, S355A or S494A substitution mutant, in which serine is replaced with alanine, to block its phosphorylation. Intriguingly, S215A, but not the other three mutants, abolished ZNF689 phosphorylation in response to IR treatment (**Fig. 2e**), suggesting that ZNF689 is phosphorylated at S215 site after DNA damage. Indeed, the phosphorylation-resistant mutant of ZNF689 (S215A) was unable to facilitate HR repair (**Supplementary Fig. 3a**). Next, to identify the specific kinase responsible for ZNF689 phosphorylation upon DNA damage, we treated MDA-MB-231 cells with selective inhibitors targeting ATM (ATMi, KU-55933, 10 μM), ATR (ATRi, Ceralasertib, 10 μM), and DNA-PKcs (DNA-PKi, NU7441, 10 μM)[33]. Interestingly, only ATMi abolished IR-induced phosphorylation of

ZNF689, whereas ATRi and DNA-PKi had no significant effect (**Fig. 2f**), suggesting that this phosphorylation event is specifically mediated by ATM. To further confirm these findings, we performed siRNA-mediated knockdown of ATM, ATR, and DNA-PKcs. Consistent with the pharmacological results, only ATM knockdown significantly reduced ZNF689 phosphorylation following IR (**Supplementary Fig. 3b and c**). Together, these results demonstrate that ATM is the primary kinase responsible for mediating DNA damage–induced phosphorylation of ZNF689.

To determine whether ZNF689 recruitment to DSBs depends on its phosphorylation, we performed ChIP assays in U2OS DR-GFP cells following siRNA-mediated ATM knockdown (**Supplementary Fig. 3d**). ZNF689 binding to DNA fragments derived from DSB sites was markedly reduced upon ATM depletion (**Supplementary Fig. 3e**), indicating that its recruitment is ATM-dependent. Additionally, IF analysis showed that WT ZNF689 formed nuclear foci concomitant with γH2AX after IR treatment, while the S215A mutant failed to do so (**Fig. 2g**), indicating that S215 phosphorylation is required for ZNF689 recruitment. Notably, ATM knockdown also reduced the recruitment of WT ZNF689 to DNA damage sites, supporting that ATM is necessary for S215 phosphorylation and ZNF689 accumulation at DNA damage foci (**Fig. 2g**). To confirm ATM directly phosphorylates ZNF689 at S215, an *in vitro* kinase assay showed strong phosphorylation of WT but not S215A ZNF689 (**Supplementary Fig. 3f**). Co-immunoprecipitation (co-IP) and *in vitro* pull-down further validated a direct interaction between ATM and ZNF689 (**Supplementary Fig. 3g and h**). Thus, these results proved that ATM phosphorylates ZNF689 at S215 in response to DNA damage, resulting in the recruitment of

ZNF689 to the sites of DNA damage.

ZNF689 directly interacts with NBS1 through its zinc-finger domains.

To test whether ZNF689 is associated with HR proteins, we performed the co-IP assay using anti-ZNF689 antibody and the results showed that ZNF689 interacts with MRN complex components, including MRE11, RAD50 and NBS1 in MDA-MB-231 and BT-549 cells (**Fig. 3a; Supplementary Fig. 4a**). But we failed to observe any interaction between ZNF689 and other HR machinery components including RAD51, RPA2 and CtIP without IR treatment (**Fig. 3a; Supplementary Fig. 4a**). The reciprocal co-IP by the antibody against MRE11, RAD50 and NBS1 confirmed the interaction between ZNF689 and MRN complex in MDA-MB-231 and BT-549 cells (**Fig. 3b; Supplementary Fig. 4b**). To further validate these interactions, we performed Stable Isotope Labeling by Amino acids in Cell culture (SILAC)-based proteomic analysis in HEK293T cells expressing Flag-ZNF689, which revealed that the interaction between ZNF689 and the MRN complex was significantly enhanced after IR (**Supplementary Fig. 4c and d**). *In vitro* pull-down assay using recombinant ZNF689, MRE11, RAD50 and NBS1 demonstrated the direct binding relationship between ZNF689 and NBS1 (**Fig. 3c and d**). However, no direct interaction was observed between ZNF689 and either MRE11 or RAD50 (**Supplementary Fig. 4e**). To further examine the association between ZNF689 and NBS1, PLA assays confirmed that IR treatment promoted their physical interaction (**Fig. 3e**). To assess their dynamic recruitment to DNA damage sites, we carried out time-lapse live-cell imaging following laser microirradiation.

Both GFP-ZNF689 and mCherry-NBS1 rapidly accumulated at irradiated sites, with recruitment detectable within 60 s and increasing over time (**Fig. 3f**). In addition, co-IP and reciprocal co-IP assays confirmed that the interaction between ZNF689 and NBS1 was strengthened after IR exposure (**Fig. 3g and h**).

ZNF689 contains 12 zinc-finger domains (ZFDs) and a Kruppel-associated box domain[17]. We next tested which region of ZNF689 is responsible for interacting with NBS1 by expressing NBS1 together with ZNF689 or its truncated mutants in HEK293T cells (**Fig. 3i**). The co-IP assay revealed that the deletion mutant of ZFDs abolished the binding of ZNF689 with NBS1 (**Fig. 3j**). Similarly, we generated deletion mutants of NBS1 (**Supplementary Fig. 5a**). The ZNF689-binding region of NBS1 was mapped to the BRCT1 domain (**Supplementary Fig. 5b**). Importantly, rescue experiments in ZNF689-deficient cells showed that both ZNF689-WT and ZNF689-ZFD were sufficient to restore HR efficiency, whereas ZNF689-ΔZFD failed to do so, indicating that the ZFDs are essential for ZNF689-mediated HR (**Fig. 3k**). Furthermore, we identified ZFD3-6 as crucial for ZNF689-NBS1 binding, with ZFD3 playing the most critical role (**Supplementary Fig. 5c and d**). Phosphorylation at S215 (located within ZFD3) enhanced ZNF689-NBS1 binding, as the S215A mutation significantly impaired this interaction, suggesting phospho-regulation of ZFD3's recruitment capacity (**Supplementary Fig. 5e**). Collectively, these results suggest that ZNF689 directly interacts with NBS1 through its zinc-finger domains.

Phosphorylation-mediated ZNF689 promotes NBS1 ubiquitination through SKP2.

Previous studies have shown that NBS1 ubiquitination promotes DSBs repair by HR[33-35]. To investigate whether ZNF689 regulates HR through this mechanism, we first observed that ZNF689 robustly promoted NBS1 ubiquitination *in vivo* (**Fig. 4a**). Consistently, in ubiquitination assays using NBS1 immunoprecipitated from cells with ZNF689 knockdown, IR-induced NBS1 ubiquitination was markedly reduced compared to control cells, indicating that ZNF689 is essential for NBS1 ubiquitination in response to DNA damage (**Fig. 4b**). The partial reduction observed upon ZNF689 knockdown also suggests that other cofactors may cooperate in this process.

K48- and K63-linked ubiquitin (Ub) chains are the most well-studied, with K48 chains regulating protein degradation. Although ZNF689 induced NBS1 ubiquitination, it did not promote NBS1 degradation (**Fig. 4a**), suggesting that ZNF689 likely induces K63- rather than K48-linked ubiquitination of NBS1. Indeed, ZNF689 WT, but not the phospho-dead mutant, enhanced K63-linked ubiquitination of NBS1 (**Fig. 4c**). Since K63-linked ubiquitination provides a docking site for protein-protein interactions[36,37], these results indicate that ZNF689 mediates the formation of K63-linked polyubiquitin chains onto NBS1.

It has been previously reported that the E3 ligases SKP2 and PELI1 directly induced the K63-linked ubiquitination of NBS1[33,35], we next determined if ZNF689 mediates NBS1 ubiquitination through SKP2 or PELI1. We found that depletion of SKP2 significantly inhibited the ZNF689-induced K63-linked ubiquitination of NBS1 (**Fig. 4d**). However, the loss of PELI1 did not affect the overall ubiquitination levels of NBS1 induced by ZNF689 (**Supplementary Fig.**

6a). Further co-IP and reciprocal co-IP assays showed that the NBS1–SKP2 interaction was reduced in ZNF689 knockout (KO) and S215A mutant cells, whereas the phospho-mimetic S215D mutant enhanced the interaction, indicating that S215 phosphorylation is required to promote NBS1–SKP2 binding (**Fig. 4e-g; Supplementary Fig. 6b-d**). Moreover, the IF assay showed that ZNF689 KO markedly reduced the number of SKP2 foci upon DNA damage (**Fig. 4h**). Expression of WT ZNF689 rescued SKP2 foci formation, whereas the phosphorylation-deficient S215A mutant did not (**Fig. 4h**). These findings suggest that ZNF689 is required for efficient SKP2 recruitment to DNA damage sites. Taken together, these results demonstrate that ATM-mediated phosphorylation of ZNF689 promotes K63-linked ubiquitination of NBS1 via the E3 ligase SKP2.

ZNF689-mediated NBS1 ubiquitination stabilizes the MRN complex and promotes ATM activation.

NBS1 ubiquitination has been shown to stabilize the MRN complex and activate ATM, facilitating the repair of DSBs through HR[33,35]. To investigate whether ZNF689-mediated NBS1 ubiquitination regulates the stability of the MRN complex upon DSB induction, we analyzed the interaction between NBS1, MRE11, and RAD50 in ZNF689-depleted cells following IR treatment. Notably, the interactions between NBS1 and both MRE11 and RAD50 were significantly diminished in ZNF689-deficient cells after IR exposure (**Fig. 5a; Supplementary Fig. 7a and b**). To further validate this recruitment at a defined chromosomal break, ChIP assays were

performed in U2OS DR-GFP cells. ZNF689 depletion markedly reduced the binding of MRE11, RAD50, and NBS1 at DSB sites (**Fig. 5b**). Previous studies have reported that SKP2 mediates NBS1 ubiquitination at the K735 residue[35]. Consistent with the importance of this modification site, we found that while NBS1 WT successfully restored MRN complex recruitment in ZNF689-depleted cells, the NBS1 K735R mutant did not (**Fig. 5b; Supplementary Fig. 7c**).

Given the essential role of the MRN complex in DNA end resection, we evaluated the effect of ZNF689 loss on DNA end resection by monitoring RPA2 foci. As expected, ZNF689 loss led to a significant decrease in RPA2 foci following IR treatment (**Fig. 5c**). Consistently, pharmacologic inhibition of MRE11 by mirin phenocopied the reduction of RPA2 foci, and mirin treatment did not further suppress RPA2 foci in ZNF689-deficient cells (**Fig. 5c**), suggesting that ZNF689 acts in the same pathway as the MRN complex to promote end resection. Consistent with the mechanism described above, overexpression of NBS1 WT restored RPA2 foci formation in ZNF689 KO cells, whereas the NBS1 K735R mutant had no such effect (**Fig. 5c**). These results suggest that ZNF689-mediated ubiquitination of NBS1 is critical for stabilizing the MRN complex and promoting DNA end resection.

We then explored the effect of ZNF689 loss on ATM activation. In ZNF689-depleted cells following IR treatment, the interaction between NBS1 and ATM was impaired (**Fig. 5d**). The levels of phosphorylated ATM (p-ATM) were significantly reduced following the loss of ZNF689 (**Fig. 5e; Supplementary Fig. 7d**). The co-localization of NBS1 with p-ATM was also significantly reduced in ZNF689 KO cells (**Fig. 5f**). Our findings confirmed that in ZNF689 KO

cells, NBS1 WT successfully restored p-ATM levels and facilitated co-localization with p-ATM, whereas the NBS1 K735R mutant was unable to achieve these effects (**Fig. 5e and f**). Importantly, ZNF689 depletion did not reduce endogenous NBS1 protein levels (**Fig. 5a**). The fact that overexpressed NBS1 WT restored MRN complex recruitment and ATM activation can be explained by the law of mass action, where high protein concentrations compensate for reduced binding affinity. Collectively, these data suggest that ZNF689-mediated NBS1 ubiquitination facilitates ATM activation at DNA damage sites and stabilizes the MRN complex, thereby promoting HR repair.

ZNF689 loss confers sensitivity to PARPi in TNBC.

Since we found that ZNF689 loss leads to HR deficiency, we sought to explore the therapeutic potential of PARPi in TNBC. We first depleted endogenous ZNF689 in MDA-MB-231 and BT-549 cells harboring WT BRCA1/2 using ZNF689-specific sgRNAs. Compared to the control group, ZNF689 KO groups were more sensitive to olaparib and exhibited significantly reduced growth after olaparib treatment (**Fig. 6a and b; Supplementary Fig. 8a and b**). Patient-derived organoid (PDO) facilitates drug tests that corroborate with patient responses[38], we thus selected three PDOs derived from TNBC patients harboring WT BRCA1/2 with diverse levels of ZNF689 expression (**Fig. 6c**). Consistent with the above results, we also found that the sensitivity of PDOs to olaparib increased along with the decrease in the ZNF689 expression level (**Fig. 6d and e**). To further validate the role of ZNF689 in DNA repair and PARPi response, we performed

gain- and loss-of-function experiments in PDOs (**Supplementary Fig. 8c**). Overexpression of ZNF689 in low-ZNF689 PDOs (PDO-3) conferred relative resistance to olaparib, whereas knockout in high-ZNF689 PDOs (PDO-1) significantly enhanced olaparib sensitivity (**Supplementary Fig. 8d and e**). Moreover, following IR, γH2AX levels were persistently elevated in ZNF689-deficient PDOs but declined over time in controls (**Supplementary Fig. 8d and e**), indicating impaired HR-mediated repair upon ZNF689 loss.

We next investigated whether olaparib exhibits therapeutic efficacy *in vivo* using MDA-MB-231, a WT BRCA1/2 model known to show modest response to PARPi[39]. We utilized xenograft tumor models inoculated with MDA-MB-231 ZNF689 WT cells and ZNF689 KO cells and found that olaparib treatment markedly inhibited the growth of ZNF689-loss MDA-MB-231 tumors in mice compared with those with high ZNF689 expression (**Fig. 6f-h; Supplementary Fig. 8f**). Furthermore, we collected two fresh TNBC tumors (TNBC-1 and TNBC-2) harboring WT BRCA1/2 with varying levels of ZNF689 expression (**Supplementary Fig. 8g and h**). We successfully established patient-derived xenograft (PDX) models (**Fig. 6i**). The PDX tumors derived from TNBC-2, which had lower ZNF689 expression than TNBC-1 (**Fig. 6j**), showed significantly greater sensitivity to olaparib than those from TNBC-1 (**Fig. 6k; Supplementary Fig. 8i**). Together, these *in vitro* and *in vivo* results support the hypothesis that ZNF689 loss is synthetic lethal with PARPi in TNBC cells.

Paclitaxel is one of the most commonly used chemotherapies in patients with TNBC[1]. Patients with defective homologous DNA repair pathways are known to be more vulnerable to

chemotherapy and PARPi treatment[40,41]. Combining PARPi with paclitaxel may provide a greater advantage in treating TNBC. Given that ZNF689 loss induces HRD, it was hypothesized that olaparib may enhance the sensitivity of TNBC tumor cells to paclitaxel. Indeed, we examined the *in vivo* combination efficacy of olaparib and paclitaxel in PDX models (**Fig. 6l**). The results showed that olaparib effectively synergized with paclitaxel *in vivo* (**Fig. 6m and n**). These findings support the therapeutic potential of olaparib in combination with paclitaxel in ZNF689 loss TNBC.

The association between ZNF689, NBS1, p-ATM, and PARPi response in clinical samples. To validate the clinical relevance of our findings, we conducted an investigation into the protein expression levels of ZNF689, NBS1, and p-ATM in a cohort of TNBC patients using tissue microarrays (TMAs) and immunohistochemistry (IHC) analysis (*n* = 269). Based on the positive staining and intensity of these three markers, the samples were categorized into high-expression and low-expression groups (**Supplementary Fig. 9a**). Our pathological analysis revealed significant positive correlations between ZNF689 levels and the expression of NBS1 and p-ATM (**Supplementary Fig. 9b**).

Given that elevated HRD scores predict better response to PARPi[42,43], we examined the association between ZNF689 expression and HRD scores in the FUSCCTNBC cohort. Our analysis demonstrated that tumors with low ZNF689 expression exhibited higher HRD scores (**Fig. 7a**). Importantly, this association was independent of BRCA mutation status, as ZNF689

expression showed no significant correlation with BRCA mutations in this cohort (**Supplementary Fig. 9c**). Moreover, in the I-SPY2 trial, TNBC tumors with low ZNF689 expression showed enhanced PARPi7 signature scores (**Fig. 7b**), indicating a potential sensitivity to PARPi[44]. To further confirm the association between ZNF689 expression and the effectiveness of PARPi, we performed IHC staining for the ZNF689 protein on pre-treatment samples obtained from seven TNBC patients who underwent PARPi therapy at our center. The results showed a significant reduction in ZNF689 expression in the three tumors that responded to PARPi (**Fig. 7c**). Taken together, these findings provide compelling evidence of a negative correlation between ZNF689 expression and the response to PARP inhibition in TNBC.

To assess the broader relevance of ZNF689 loss, we found that its depletion in luminal breast cancer (MCF7, T47D, ZR-75-1), ovarian (OVCAR8), prostate (LNCaP), and pancreatic (BxPC-3) cell lines markedly increased DNA damage and enhanced sensitivity to PARP inhibition (**Supplementary Fig. 10a-f**). In contrast, non-tumorigenic epithelial cells (MCF10A and HMEC) did not exhibit such effects (**Supplementary Fig. 10g and h**). In addition, pan-cancer analysis of TCGA data revealed that low ZNF689 expression was associated with HRD or PARPi sensitivity signatures across multiple cancer types, including pancreatic and prostate cancer, but not ovarian cancer (**Supplementary Fig. 11a-e**). These findings suggest that ZNF689 may serve as a context-dependent regulator of HR and a predictive biomarker for PARPi response beyond TNBC.

PARPi upregulates PD-L1 expression more potently in ZNF689-deficient TNBC via activating the STING pathway.

Previous studies have shown that PARP inhibition upregulates PD-L1 expression and enhances cancer-associated immunosuppression through cGAS/STING signaling in TNBC[45]. To investigate this, we first assessed PD-L1 levels with and without ZNF689 KO following PARPi treatment. Interestingly, olaparib significantly increased PD-L1 expression at the surface, mRNA, and protein levels in ZNF689-deficient MDA-MB-231 cells (**Fig. 7d-f**). Consistently, a more pronounced increase in PD-L1 levels was observed in ZNF689-deficient MDA-MB-231 xenografts (**Fig. 7g**). Next, we examined cGAS/STING activation in ZNF689 KO MDA-MB-231 cells. ZNF689 deficiency led to an increase in intracellular 2'3'-cGAMP (cGAMP) levels (**Fig. 7h**), a cyclic dinucleotide produced by cGAS that activates STING and promotes IRF3-mediated transcription[46]. Olaparib treatment further enhanced the activation of the STING/TBK1/IRF3 pathway in ZNF689-deficient MDA-MB-231 cells (**Fig. 7i**). Moreover, a higher proportion of ZNF689-KO MDA-MB-231 cells contained micronuclei positive for the cytoplasmic DNA sensor cGAS (**Fig. 7j**), aligning with the notion that micronuclear DNA is recognized by cGAS. Activation of the STING pathway in tumor cells promotes the production of pro-inflammatory cytokines in response to PARPi[47]. Notably, olaparib induced a stronger production of IFN-β, CCL5, and CXCL10 in ZNF689-deficient MDA-MB-231 cells (**Fig. 7k and l**). Furthermore, depletion of either cGAS or STING reduced the expression of PD-L1 (**Supplementary Fig. 12a-e**) and inflammatory genes (IFN-β, CCL5, and CXCL10) (**Supplementary Fig. 12f and g**) in ZNF689-

deficient cells. Collectively, these results indicate that PARPi upregulates PD-L1 expression more potently in ZNF689-deficient TNBC by activating the STING pathway.

PARPi enhances the therapeutic efficacy of PD-L1 blockade in ZNF689-deficient TNBC. Building on our observations that PARP inhibition significantly upregulates PD-L1 in ZNF689-deficient TNBC, we established 4T1 ZNF689 KO xenograft tumors in BALB/c mice to explore whether combining PARP inhibition with PD-L1 blockade might enhance therapeutic efficacy (**Fig. 8a**). Notably, ZNF689 deficiency synergized with both PARPi and anti-PD-L1 treatments, leading to a significant reduction in 4T1 tumor growth (**Fig. 8b and c; Supplementary Fig. 13a and b**). Additionally, we used flow cytometry to analyze the immune response within the tumors post-treatment. The combined therapy resulted in a higher infiltration of $CD4^+$ and $CD8^+$ T cells and elicited a robust immune response characterized by an increased proportion of $GZMB^+$ $CD8^+$ and IFN-γ^+ $CD8^+$ T cells compared to monotherapy alone (**Fig. 8d; Supplementary Fig. 13c**). Similar results were observed in the C57BL/6 mouse model using AT3 cells (**Supplementary Fig. 13d-h**). These findings indicate that combining PARP inhibition with PD-L1 blockade induces a potent T cell-mediated anti-tumor immunity in ZNF689-deficient TNBC.

We utilized a patient-derived tumor fragment (PDTF) platform[48] to test if combining PARPi with anti-PD-L1 therapy enhances the response in TNBC (**Fig. 8e**). Tumor samples from ten TNBC patients were stratified into high (top five) and low (bottom five) ZNF689 expression groups based on western blot analysis (**Supplementary Fig. 13i**). PDTFs from these samples

were treated with anti-PD-L1, with or without olaparib. Flow cytometry showed that in the low ZNF689 expression group, the combination therapy significantly increased T cell activation markers ICOS, CD137, and CD25 (**Fig. 8f**). Additionally, this group exhibited higher levels of IFN-γ and TNF-α, indicating a strong immune response (**Fig. 8g**). These results suggest that the combination therapy induces a rapid reprograming of tumor microenvironment, enhancing T cell activity, and may be effective for treating ZNF689-deficient TNBC.

Discussion

In this study, we established that ZNF689 loss impairs HR repair and increases the response of TNBC cells to PARPi. Mechanistically, ZNF689 is activated by ATM-mediated phosphorylation and is recruited to sites of DNA damage in an ATM-dependent manner. ZNF689 interacts with NBS1 to promote K63-linked ubiquitination of NBS1 by enhancing its interaction with the E3 ligase SKP2. This ubiquitination stabilizes the MRN complex, enhancing ATM activation and accelerating HR repair. In ZNF689-deficient TNBC, PARP inhibition significantly upregulates PD-L1 expression and enhances the efficacy of PD-L1 blockade by activating the cGAS/STING pathway, which promotes $CD8^+$ T-cell recruitment and boosts antitumor activity (**Fig. 8h**).

BRCA1 and BRCA2 are vital for genome integrity via HR[49]. Mutations in these genes impair DSB repair, leading to chromosomal instability and increased breast cancer risk[50]. Although PARPis have received approval for treating HER2-negative breast cancer associated with BRCA1/2 mutations[5,7,40], their therapeutic application has not yet been authorized for patients without BRCA mutations. Hence, strategies that selectively disrupt HR in cancer cells hold promise for extending benefit of PARPi to patients with BRCA-WT[51]. Our study identifies ZNF689 as an essential component of the HR repair machinery in TNBC. Previously characterized as a transcription factor linked to various malignancies[17,52-54], ZNF689 has been shown in our prior research to limit intratumor heterogeneity in breast cancer by inhibiting LINE-1 retrotransposition[20]. These findings complement our previous work, which showed that ZNF689 deficiency promotes immunotherapy resistance via increased intratumoral

heterogeneity, by demonstrating a distinct, context-dependent role of ZNF689 in HR repair and sensitization to PARPi and immune checkpoint blockade. Its role in DNA damage repair in breast cancer had not been investigated until now. Notably, consistent with its function as a transcription factor, we also noted that ZNF689 depletion leads to the downregulation of multiple HR genes. Therefore, we cannot exclude the possibility that this transcriptional downregulation may also be contributory to the observed HR defects, acting in concert with its direct role in the DDR.

Our findings reveal ZNF689's critical role in regulating HR repair in TNBC, suggesting an important HR regulatory pathway. *In vitro* and *in vivo* assays confirm that ZNF689-deficient TNBC tumor cells with BRCA-WT are more sensitive to PARPi. Furthermore, our findings in non-TNBC models demonstrate that ZNF689 also functions as a context-dependent regulator of HR repair. While our current study focuses on the pronounced HR dependency in TNBC, these collective results suggest that ZNF689 plays a conserved role in maintaining genomic stability across various cancer types. Therefore, our study provides deeper insights into HR regulation and highlights the potential of ZNF689 loss as a predictive biomarker for PARPi response, both in BRCA-WT TNBC patients and potentially beyond the TNBC context.

ATM is the apical kinase responsible for global orchestration of cellular responses to DSBs[8,55]. To fulfil this function, ATM phosphorylates hundreds of substrates in response to DNA damage[8]. In this study, we have identified ZNF689 as a previously unrecognized substrate of ATM. Specifically, ATM directly phosphorylates ZNF689 at its S215 upon DNA damage, directing its recruitment to DSB sites. Phosphorylation-resistant mutant of ZNF689 (S215A) failed to

localize to the sites of DNA damage, indicating the importance of ATM-dependent recruitment of ZNF689 for its function in HR repair. Notably, ZNF689-mediated NBS1 ubiquitination is essential for the activation of ATM at DSB sites. Therefore, ZNF689 and ATM mutually affect each other through a positive feedback loop in promoting HR repair.

NBS1 is a multifunctional protein involved in various DDR pathways, including the recognition and repair of DSBs, cell cycle checkpoint activation, and telomere maintenance[56]. One of the primary functions of NBS1 is its involvement in the recognition and repair of DSBs. NBS1 acts as a sensor of DSBs, initiating the DNA damage signaling cascade and recruiting the MRN complex to the site of damage[57]. The MRN complex plays a critical role in processing DNA ends and facilitating their repair through HR or NHEJ[58,59]. In this study, we demonstrate that ZNF689 triggers K63-linked ubiquitination of NBS1 via the E3 ligase SKP2 when exposed to genotoxic stress. While ubiquitination is typically linked to protein degradation, recent studies indicate that NBS1 ubiquitination plays a critical role in ATM activation and HR repair following DNA damage[33-35]. Our study reveals that ZNF689-mediated NBS1 ubiquitination acts as a scaffold, stabilizing the MRN complex and facilitating the recruitment of ATM to DNA damage foci, subsequently activating ATM. Importantly, since SKP2 is dispensable for basal MRN formation[35], ZNF689 may stabilize the complex independently of NBS1 ubiquitination. Furthermore, because MRE11 and RAD50 lack ubiquitin-binding domains, NBS1 ubiquitination likely primarily drives its recruitment to DSBs[34], aligning with our observed recruitment defects. Once recruited to the damage sites, we propose that ZNF689 functions as a damage-induced

structural brace for the MRN complex. During active DNA repair, the extensive, ATP-driven conformational rearrangements of RAD50 and MRE11 impose significant conformational strain. ZNF689 is specifically required after IR to reinforce the complex against the physical demands of end resection, a requirement absent in the latent, undamaged MRN complex. Given that MRN assembly is a prerequisite for recruiting CtIP to drive DNA end resection[57,60], ZNF689 likely supports this step by maintaining MRN integrity. Thus, the resection defects in ZNF689-deficient cells are likely a downstream consequence of MRN destabilization, establishing ZNF689 as an upstream regulator of the resection machinery. Notably, the DNA end resection defect observed upon ZNF689 loss appears more severe than the corresponding reduction in HR efficiency. This suggests that ZNF689 may possess additional roles in promoting DNA resection that are partially independent of the core HR pathway, such as facilitating extensive resection beyond what is strictly required for HR, or functioning at non-HR genomic sites.

PARPis have revolutionized the treatment of patients with BRCA1/2-associated breast cancer, representing a pioneering targeted therapy capable of improving outcomes in patients with hereditary tumors[61-64]. They are primarily investigated in combination with other therapies for various solid tumors[14]. However, questions remain about the optimal use of PARPi, including whether to use them in combination or as standalone maintenance therapy, and if in combination, which drugs are best paired with PARPi[65,66]. Our research demonstrates that combining PARPi with paclitaxel, a widely used chemotherapeutic agent for TNBC, is a promising therapeutic strategy in the context of ZNF689-deficient TNBC. These findings suggest an immediately

applicable treatment strategy for TNBC. Nonetheless, the precise mechanisms underlying the synergy between PARPi and paclitaxel in ZNF689-deficient TNBC require further investigation. Furthermore, PARPi markedly increased PD-L1 expression in ZNF689-deficient TNBC, enhancing the effectiveness of PD-L1 blockade by activating the cGAS/STING pathway and promoting $CD8^+$ T-cell recruitment, thus boosting antitumor activity. Preclinical studies confirm that combining PARPi with immunotherapy enhances immune response and synergistically inhibits tumor growth[47,67]. In clinical settings, numerous trials have investigated the combination of PARP inhibition with immune checkpoint blockade in TNBC and other cancers[68-72]. Our findings uncover an uncharacterized mechanism for PARPi and provide additional rationale for their combination with immunotherapies in treating TNBC, irrespective of BRCA mutation status.

This study has several limitations. The precise mechanism by which S215 phosphorylation of ZNF689 influences NBS1 interactions with MRE11/RAD50 and SKP2 remains unclear. Given that BRCT domains are known to bind phosphopeptides, it is possible that phosphorylation at S215 induces the interaction with the BRCT domains of NBS1. We speculate that phosphorylation may induce conformational changes in NBS1, enhancing MRN complex assembly or SKP2 binding. However, this hypothesis awaits further structural validation.

In summary, our study not only identifies unrecognized functions of nuclear protein ZNF689 in HR-mediated DNA repair, but also demonstrates that PARPi alone or combined with anti-PD-L1 immunotherapy could be potential treatment options for patients with TNBC exhibiting low ZNF689 expression.

Methods

Ethical statement

We confirm that this research complies with all relevant ethical regulations. The collection and use of patient-derived clinical samples were reviewed and approved by the Ethics Committee of Fudan University Shanghai Cancer Center (FUSCC), and written informed consent was obtained from all participants. All animal experiments were performed in accordance with the protocols authorized by the FUSCC Institutional Animal Care and Use Committee (FUSCC-IACUC-2022114).

Cell lines

Human cancer cell lines, including MDA-MB-231 (Cat# HTB-26; female), BT-549 (Cat# HTB-122; female), MCF7 (Cat# HTB-22; female), T47D (Cat# HTB-133; female), ZR-75-1 (Cat# CRL-1500; female), LNCaP (Cat# CRL-1740; male), and U2OS (Cat# HTB-96; female), as well as HEK293T cells (Cat# CRL-3216; female), non-tumorigenic epithelial cell lines MCF10A (Cat# CRL-10317; female) and HMEC (Cat# PCS-600-010; female), and the murine mammary carcinoma cell line 4T1 (Cat# CRL-2539; female), were obtained from the American Type Culture Collection (ATCC). The human ovarian cancer cell line OVCAR8 (Cat# YC-B082; female) and the murine mammary carcinoma cell line AT3 (Cat# YC-A159; female) were obtained from Ubigene. All cell lines were maintained under standard culture conditions, routinely authenticated via short tandem repeat (STR) profiling, and regularly tested for *Mycoplasma*

contamination.

Chemical products

The following chemicals were purchased from Selleck: KU-55933 (ATM inhibitor, Cat# S1092), ceralasertib (ATR inhibitor, Cat# S7693), NU7441 (DNA-PKcs inhibitor, Cat# S2638), mirin (MRE11 inhibitor, Cat# S8096), olaparib (PARP inhibitor, Cat# S1060), and paclitaxel (Cat# S1150).

Plasmid construction, siRNA, sgRNA and transfection

Plasmids for Flag-ZNF689 (WT, S215A, S215D, S221A, S355A, S494A), Flag-ZNF689 truncation mutants (ZFD, △ZFD, △ZFD1-12), HA-NBS1 (WT, K735R) and HA-NBS1 truncation mutants (△FHA, △BRCT1, △BRCT2, △MA, △C) were synthesized by Synbio Technologies (Suzhou, China). Plasmid transfections were conducted using Lipofectamine 2000 (Invitrogen). siRNAs were obtained from RiboBio (**Supplementary Table 2**) and transfected into cells using Lipofectamine RNAiMAX (Invitrogen). The lentivirus-mediated CRISPR/Cas9 KO vector targeting human or mouse ZNF689 was also sourced from Synbio Technologies (Suzhou, China). Refer to **Supplementary Table 3** for gRNA sequences. Cells at 30% confluence were incubated in a medium containing optimal dilution of lentivirus mixed with polybrene. Following 48 h of transfection, cells underwent puromycin selection to establish stable transfected cell lines.

RNA isolation and real-time quantitative reverse transcription (RT-qPCR)

Total RNA was extracted with the RNeasy kit (QIAGEN) and converted into cDNA using the HiScript III RT SuperMix with gDNA wiper (Vazyme). RT-qPCR was conducted with ChamQ SYBR qPCR Master Mix (Vazyme) on a 7900HT Fast Real-Time PCR System (Applied Biosystems). Primer sequences are listed in **Supplementary Table 4**.

RNA-seq and data analysis

Total RNA from MDA-MB-231 cells (transfected with control or ZNF689 siRNA; *n* = 3 biological replicates) was extracted using the RNeasy kit (QIAGEN). RNA-seq library preparation and sequencing were performed at Shanghai Majorbio Bio-Pharm Technology Co., Ltd. using the HiSeq-2500 platform (Illumina). Raw sequencing reads were aligned to the human reference genome (hg38) using HISAT2, and transcript abundance was quantified as fragments per kilobase million (FPKM) using Cufflinks. GSEA was conducted using the GSEA v4.2 desktop application.

HR and NHEJ repair assays

Cells integrated with DR-GFP or EJ5-GFP cassettes were utilized to assess HR or NHEJ efficiency, respectively[73]. Cells transiently transfected with indicated plasmids or siRNA were then transfected with I-SceI expression vector pCBASceI (Addgene). After 48 h, GFP-positive

cells were quantified via flow cytometry. HR or NHEJ efficiency was expressed as a percentage relative to control cells.

Cell cycle analysis

Cells were harvested, washed with ice-cold phosphate-buffered saline (PBS), and fixed in 70% ethanol overnight at 4°C. After PBS washing, cells were treated with RNaseA at room temperature for 60 min, followed by the addition of propidium iodide for flow cytometry analysis.

Irradiation

Cells were exposed to IR at 6 Gy for PLA and IF assays, and at 10 Gy for western blot, co-IP, and metaphase spread analyses. Unless otherwise indicated, cells were collected 4 h post-irradiation for PLA and IF, 1 h for western blot and co-IP, and 2 h for metaphase spread analyses.

Metaphase spread assay

MDA-MB-231 cells were transfected with control or ZNF689 siRNA, followed by 10 Gy IR treatment. 2 h post-IR, cells were treated with 100 ng/mL colcemid (Gibco) for 3 h, then suspended in 0.56% KCl for 15 min at 37°C. The cells were fixed in methanol/acetic acid (3:1) for 20 min, spread onto slides, and dried at room temperature. Slides were then mounted with DAPI (Beyotime) and analyzed using a Leica DMi8 microscope (Leica Microsystems).

ZNF689 WT and S215A protein purification

The open reading frames (ORFs) of human ZNF689 WT and S215A were sub-cloned into modified pCAG vector. The plasmid was transfected to suspension Expi293F cells using PEI. After culture at 37 °C, 5% CO_2 for 3 days, cells were collected and lysed in 30 mM HEPES (pH 8.0), 300 mM NaCl, 0.25% CHAPS, 5 mM ATP, 5 mM $MgCl_2$, 10% Glycerol and 2 mM DTT at 4 °C for 30 min, and the insoluble fraction was removed by centrifugation at 38,000 × g for 30 min. Supernatants were incubated with IgG antibody-agarose for 4 h and washed extensively. The fusion proteins were digested using ULP1 protease and then eluted with PBS buffer.

ATM protein purification

The ORF of human ATM was codon-optimized and sub-cloned into modified pCAG vector. The plasmid was transfected to suspension Expi293F cells using PEI. After culture at 37 °C, 5% CO_2 for 3 days, cells were collected and lysed in 50 mM HEPES (pH 7.4), 400 mM KCl, 20mM NaCl, 20% glycerol, 10 mM $MgCl_2$, 0.5 mM PMSF, 1 mM TCEP, 5 mM ATP, 10 mM NaF, 1 μg/mL Aprotinin/Pepstanin/Leupetin at 4 °C for 30 min, and the insoluble fraction was removed by centrifugation at 38,000 × g for 30 min. Supernatants were incubated with IgG antibody-agarose for 4 h and washed extensively. The fusion proteins were digested using 3C protease and then eluted with 25 mM HEPES 7.4, 400 mM KCl, 15% glycerol, 10 mM $MgCl_2$, 1 mM TCEP buffer.

Pull-down assays

Fusion proteins (ZNF689, MRE11, RAD50, and NBS1) were purchased from Proteintech. For GST pull-down, 2 μg of GST-tagged protein was incubated with 2 μg of His-tagged binding partner and an anti-GST antibody in binding buffer (50 mM Tris-HCl, pH 7.5, 150 mM NaCl, 0.05% NP-40, and protease inhibitor cocktail) overnight at 4 °C, followed by incubation with Dynabeads Protein A/G (Invitrogen) for 1 h. For His pull-down, 2 μg of His-tagged protein was incubated with 2 μg of GST-tagged partner and Ni-NTA agarose beads (Qiagen) in the same buffer overnight at 4 °C. Beads were washed five times and eluted by boiling in SDS loading buffer for 5 min. For ATM pull-down, purified recombinant ATM protein was pre-bound to anti-ATM antibody-conjugated Protein A/G agarose beads in binding buffer (20 mM Tris-HCl, pH 7.5, 150 mM NaCl, 1 mM EDTA, 0.1% NP-40, and protease inhibitors) at 4 °C for 1 h with gentle rotation. Flag-ZNF689 protein was then added and incubated for an additional 2 h. Beads were washed three times and eluted in SDS loading buffer by boiling.

***In vitro* ATM kinase assay**

Briefly, 10 ng of purified constitutively active ATM was incubated in kinase reaction buffer with 1 μg of recombinant ZNF689 WT or S215A mutant protein. The reaction was initiated by adding 250 μM ATP supplemented with magnesium and manganese acetate, and allowed to proceed at room temperature for 1 h. The reaction was terminated using the ADP-Glo Kinase Assay kit (Promega), and luminescence was measured using a Synergy 4 plate reader (BioTek) according to the manufacturer's instructions.

Clonogenic cell-survival assay

MDA-MB-231 and BT-549 cells were treated with specified doses of olaparib and seeded into 6-well plates (500 cells per well). After 12 days, viable cells were fixed and stained with 0.25% crystal violet. Colonies with more than 50 cells were counted.

EMSA

The DNA-binding ability of ZNF689 was assessed by EMSA. Biotin-labeled oligonucleotides corresponding to blunt-end, 3' overhang, 5' overhang, and single-stranded DNA were synthesized based on the sequences listed in **Supplementary Table 5**. A common strand (JYM696) was annealed with specific complementary oligonucleotides to generate the respective double-stranded probes; single-stranded DNA consisted of JYM696 alone.

Binding reactions were carried out in a 20 μl volume containing 25 mM MOPS (pH 7.0), 50 mM KCl, 1 mM DTT, 1 mM $MnCl_2$, 1-2 nM biotin-labeled DNA probe, and recombinant ZNF689 protein at the indicated concentrations. After 15 min incubation at room temperature, samples were resolved by 6% native polyacrylamide gel electrophoresis in 0.5 × TBE buffer. DNA-protein complexes were transferred to a positively charged nylon membrane and detected using a chemiluminescent EMSA kit (Beyotime). Signals were visualized using an Amersham Imager 600 (GE Healthcare).

Western blotting and co-IP assays

Western blotting was conducted using standard methods, with protein expression quantified via ImageJ as the ratio of test protein to internal control. Antibody details are in **Supplementary Table 6**. For co-IP, cells were lysed in RIPA buffer (50 mM Tris pH 7.4, 150 mM NaCl, 1% NP-40, 0.25% sodium deoxycholate, protease inhibitor cocktail). Lysates were incubated with indicated antibodies overnight at 4°C, followed by precipitation with Dynabeads Protein A/G (Invitrogen) for 2 h, washed five times with lysis buffer, and eluted with SDS loading buffer by boiling for 5 min.

PLA

PLA was performed using the Duolink In Situ Red Starter Kit Mouse/Rabbit (Sigma-Aldrich) according to the manufacturer's instructions. Briefly, MDA-MB-231 cells seeded onto glass slides, fixed with 4% paraformaldehyde, and permeabilized with 0.2% Triton X-100. After blocking, cells were incubated with primary antibodies overnight at 4 °C, followed by incubation with PLA probes (PLUS and MINUS) for 1 h at room temperature. Ligation and rolling circle amplification were carried out using the supplied reagents, nuclei were counterstained with DAPI (Beyotime), and images were acquired with a Leica DMi8 confocal microscope (Leica Microsystems). Detailed antibody information is provided in **Supplementary Table 6**.

Laser micro-irradiation, imaging, and IF

DSBs were induced using a high-resolution spinning disk confocal microscope equipped with the cellFRAP photomanipulation system (Spin SR, Olympus). MDA-MB-231 cells were transfected with GFP-ZNF689 and mCherry-NBS1 expression plasmids and seeded onto glass-bottom dishes (NEST). At 24 h post-transfection, cells were incubated with 10 μM 5-bromo-2'-deoxyuridine (BrdU, Selleck) for 24 h prior to laser microirradiation. Laser-induced DSBs were generated using a 405 nm fixed-wavelength ultraviolet laser in a temperature-controlled chamber, with the following parameters: 20% laser intensity, 0.2 s exposure per 5 scan lines, using a ×100 oil immersion objective.

For IF, cells grown on glass coverslips were fixed with 4% paraformaldehyde, permeabilized with 0.2% Triton X-100, and blocked with 10% normal goat serum in PBS. Primary antibodies were incubated overnight at 4°C, followed by three PBS washes and incubation with fluorescent secondary antibodies. After nuclear staining with DAPI (Beyotime), coverslips were mounted and imaged using a Leica DMi8 microscope (Leica Microsystems). Colocalization analysis was performed using Leica LAS X software. Detailed antibody information is provided in **Supplementary Table 6**.

IHC

Human TMAs containing primary tumor samples from 269 female patients with TNBC, as well as pre-treatment tumor tissue sections from seven female TNBC patients who received PARPi therapy, were obtained from FUSCC. IHC staining was performed on representative formalin-

fixed, paraffin-embedded (FFPE) tissue sections from both the human TNBC cohorts and mouse tumor xenografts using the following antibodies: anti-ZNF689, anti-NBS1, anti-p-ATM, and anti-PD-L1. The immunoreactivity scores were calculated by multiplying the staining intensity (0 = negative, 1 = weak, 2 = moderate, 3 = strong) by the percentage of positive staining (0 = 0%, 1 ≤ 10%, 2 = 11–50%, 3 > 50%). Low and high expression groups were defined according to the median immunoreactivity score. Details on the antibodies used are provided in **Supplementary Table 6**.

ChIP-PCR

U2OS DR-GFP cells, carrying a chromosomal integrated single-copy of I-SceI site, were used to detect protein recruitment to I-SceI endonuclease-induced DSB sites. Cells were transfected with I-SceI plasmids to introduce DSBs. After 48 h, a ChIP assay was performed using the SimpleChIP® Enzymatic Chromatin IP kit (Cell Signaling Technology) according to the manufacturer's instructions. DNA associated with ZNF689, MRE11, RAD50, or NBS1 was detected by PCR with primers targeting the I-SceI site. The primer sequences were: forward, 5'-TACAGCTCCTGGGCAACGTG-3'; reverse, 5'-TCCTGCTCCTGGGCTTCTCG-3'. The PCR conditions were: 95 °C for 5 min (1 cycle); 95 °C for 45 s, 56 °C for 30 s, 72 °C for 30 s (35 cycles); and 72 °C for 10 min (1 cycle). The amplified products were analyzed on a 1.2% agarose gel.

SILAC-based quantitative proteomic analysis

ZNF689 interactomes were analyzed using a 3-plex SILAC approach (*n* = 1 biological replicate per condition; 3 samples pooled into one multiplexed run). Briefly, HEK293T cells expressing vector control (light: Lys0/Arg0) or Flag-ZNF689 (medium: Lys4/Arg6; heavy: Lys8/Arg10, treated with 10 Gy IR for 1 h recovery) were subjected to anti-Flag immunoprecipitation. Proteins were resolved by SDS-PAGE and in-gel digested with trypsin[74]. Desalted peptides were analyzed on a NanoElute 2 LC system coupled to a TimsTOF Pro 2 mass spectrometer (Bruker Daltonics). Separation was performed on an AUR3-15075C18 column (IonOpticks) at 400 nL/min using a 60-min gradient (2.2% to 90% buffer B). The instrument operated in DDA-PASEF mode with 10 PASEF scans per cycle, acquiring MS/MS spectra over a 100–1700 m/z range and an ion mobility range of 0.6–1.6 V·s/cm².

Raw MS files were processed using MaxQuant (v2.6.7.0)[75] against the Human UniProtKB database (UP000005640). The false discovery rate (FDR) was strictly controlled at 1% for both proteins and peptides. For statistical validation, the “ProteinGroups.txt” output was imported into Perseus (v2.1.4.0)[76]. Specific interacting proteins were identified using the Significance B test ($P < 0.05$), which evaluates whether a protein’s SILAC ratio significantly deviates from the background distribution binned by protein intensity. The quantified ZNF689-associated proteins are listed in **Supplementary Data 1**.

Ubiquitination assay

For the cellular ubiquitination assay, HEK293T cells were transfected with the specified plasmids for 48 h and then harvested using a denaturing buffer (6 M guanidine-HCl, 0.1 M Na_2HPO_4/NaH_2PO_4, and 10 mM imidazole). Prior to immunoprecipitation, the denatured cell extracts were diluted with a non-denaturing lysis buffer to restore conditions amenable to antibody binding. The cell extracts were incubated with the target antibody for 3 h, washed, and analyzed by western blot.

Cell survival assay

To assess the effect of olaparib on TNBC viability, cells were grown in 96-well plates at 2×10^3 cells per well and exposed to different concentrations of olaparib. After 72 h, the cells were incubated with 10% CCK-8 (Vazyme) solution at 37 °C for 2 h. The cell survival percentages at different concentrations were calculated by dividing the optical density (OD) of chemical-containing wells by that of DMSO-contacting wells.

PDO

Fresh breast cancer tissues were minced into 1-2 mm fragments and digested with collagenase and hyaluronidase in a digestion buffer (DMEM/F12 with 5% bovine serum albumin, insulin, and hydrocortisone) for 2 h at 37°C. The tissue was then centrifuged at 350 g for 5 min. The samples were resuspended in 10 mL of digestion buffer and passed through a 100 μm cell strainer (Corning). After centrifugation at 350 g for 5 min, the pellets were resuspended in digestion

buffer and centrifuged again. Cell clusters were then resuspended in BME type-2 buffer (Trevigen) and seeded onto a 12 mm, 0.4 μm inner Transwell chamber (Corning) precoated with Matrigel. The suspension was solidified by incubating for 30 min at 37°C and 5% CO_2 with 1 mL of breast cancer organoid medium[38]. The culture medium was replaced every 2-3 days. ZNF689 overexpression and KO PDOs were generated using a lentiviral transduction system. Concentrated lentiviruses were mixed 1:1 with Matrigel, and organoids were embedded and cultured in culture medium. At 72 h post-transduction, 2 μg/mL puromycin was added for 1 week to select transduced cells, after which surviving organoids were used for subsequent experiments. For olaparib treatment, organoids in good condition were harvested, dissociated into single cells, and cultured with olaparib for 1 week. Cell viability was then assessed using the CellTiter-Glo 3D cell viability assay (Promega) according to the manufacturer's instructions. Photos were taken on the last day to observe changes in the organoids under drug treatments.

Animal studies

All animal procedures were carried out in the specific pathogen-free (SPF) facility at FUSCC. Female mice were housed at 20–23 °C and 50–60% humidity with a 12-hour light/dark cycle and free access to food and water. To ensure objectivity, investigators were blinded to treatment allocations during data collection and analysis. Tumor dimensions and body weights were recorded every 3 days. Tumor volume (V) was calculated using the formula $V = (\text{width}^2 \times \text{length})/2$. The maximal tumor burden permitted by the FUSCC-IACUC is 2000 mm^3, and we

confirm that this limit was not exceeded in any experimental procedures.

To evaluate the effect of ZNF689 on *in vivo* olaparib sensitivity, 24 female NOD/SCID mice (5–6 weeks old, n = 6/group) were orthotopically injected with 1×10^6 MDA-MB-231 cells (sgCtrl or sgZNF689) into the mammary fat pads (MFPs). Once average tumor volumes reached 100 mm^3, mice were randomized to receive vehicle or olaparib (50 mg/kg) via intraperitoneal (i.p.) injection, 5 days per week for 3 weeks.

For PDX studies, 24 female NSG mice (5–6 weeks old, n = 6/group) were orthotopically engrafted with TNBC-1 or TNBC-2 tumor fragments. Treatment began when tumors reached ~100 mm^3 with either vehicle or olaparib (50 mg/kg, i.p., 5 days per week for 4 weeks). For the synergy assessment, 24 female TNBC-2 PDX-bearing NSG mice were randomized into four groups: vehicle, paclitaxel (20 mg/kg, i.p., 6 doses total, every other day), olaparib (50 mg/kg, i.p., 5 days per week), or the combination of both.

To investigate the efficacy of dual PARP and PD-L1 inhibition, we utilized female BALB/c (n = 6/group) and C57BL/6 mice (n = 5/group), all 5–6 weeks old. Mice were orthotopically challenged with 1×10^5 4T1 or AT3 sgZNF689 cells. At a tumor volume of ~100 mm^3, a 2-week treatment was initiated: IgG control (100 μg, i.p., every 3 days), anti-PD-L1 antibody (100 μg, i.p., every 3 days), olaparib (50 mg/kg, i.p., 5 days per week), or the combination regimen.

Flow cytometry analysis

Freshly excised tumors were collected postmortem and enzymatically digested in a solution

containing 0.5 mg/mL collagenase type I (Sigma-Aldrich), 1 mg/mL dispase (Roche), and 1 mg/mL hyaluronidase (Sigma-Aldrich), supplemented with antibiotics. Digestion was carried out at 37°C for 1 h. The digested tissues were filtered through a 40-μm strainer to yield single-cell suspensions, followed by red blood cell lysis for 10 min at room temperature. For surface marker analysis, single-cell suspensions were incubated with the appropriate fluorochrome-conjugated antibodies for 30 min at 4°C in the dark. For intracellular staining of mouse GZMB and IFN-γ, cells were pre-stimulated with Leukocyte Activation Cocktail (BD Biosciences) for 6 h, followed by surface and intracellular staining using the Cytofix/Cytoperm kit (BD Biosciences). A viability dye was included to distinguish live from dead cells. All antibodies used for flow cytometry are listed in **Supplementary Table 6**. Data were acquired and analyzed using CytExpert software (Beckman Coulter).

PDTF cultures and analysis

Tissue samples designated for PDTF cultures were meticulously processed into 1-2 mm^3 fragments. These fragments were then embedded in a tailored artificial extracellular matrix combined with Matrigel, and allocated within a 96-well plate. After stabilization at 37°C, they received a tumor medium supplemented with either atezolizumab or olaparib. After incubation for 48 h, the PDTFs were readied for flow cytometry. This procedure aimed to evaluate T-cell activation using designated antibodies, including ICOS, CD137, and CD25. Subsequently, the PDTFs were isolated, subjected to enzymatic digestion, and transformed into single-cell

suspensions. After a blocking phase, these cells were stained and analyzed. Moreover, 48 h after culture, supernatants from the PDTF cultures underwent analysis to determine IFN-γ and TNF-α levels, using the ELISA kits (Lianke) following the manufacturer's guidelines.

Calculation of HRD score

Unadjusted loss-of-heterozygosity (LOH), telomeric allelic imbalances (NtAI), large-scale transitions (LST), and tumor ploidy were estimated using the scarHRD R package[77]. For the TCGA dataset, the HRD score was defined as the unweighted sum of LOH, NtAI, and LST. For the FUSCCTNBC cohort, to account for ploidy effects[78], the HRD score was calculated as the sum of LOH, NtAI, and a ploidy-adjusted LST score (LSTm = LST - 15.5 × ploidy).

cGAMP assay

For intracellular 2'3'-cGAMP quantification, MDA-MB-231 cells were seeded in 6-well plates. At 80-90% confluency, cells were washed twice with PBS, trypsinized, and collected by centrifugation. Cell pellets underwent three cold PBS washes to remove phenol red, with all steps on ice. Pellets were resuspended in protein extraction buffer and incubated for 5 min with gentle shaking. Whole-cell lysates were centrifuged, and the supernatant was used for cGAMP quantification via ELISA (Cayman Chemical) per the manufacturer's instruction. Protein concentration was determined and used to normalize cGAMP levels across samples.

Targeted sequencing of BRCA1/2

Genomic DNA was extracted and quantified using the Qubit® dsDNA HS Assay Kit (Thermo Fisher Scientific). Targeted sequencing libraries were prepared using the GenSeizer MJ2020 BRCA I/II Panel (Maojin), which amplifies all exons and splice junctions of BRCA1 and BRCA2 through multiplex PCR. Following two rounds of PCR amplification and AMPure XP bead (Beckman Coulter) purification, libraries were quantified and pooled for sequencing. Paired-end sequencing (PE150) was performed on the DNBSEQ-G99 platform (BGI Genomics). Raw sequencing reads were quality-filtered using fastp, aligned to the human reference genome (hg19) using BWA-MEM, and variant calling was performed using VarDict in amplicon mode. Variants were annotated with ANNOVAR.

Statistics and reproducibility

The statistical details and methods are indicated in the figure legends or supplementary information. Statistical analyses were performed using R software (v4.1.3) or GraphPad Prism (v8.0.1). Statistical significance was evaluated using two-tailed unpaired Student's *t*-tests, one- or two-way ANOVA, Spearman correlation, two-tailed Wilcoxon tests, Pearson's chi-squared tests, or MANOVA, as denoted in the respective figure legends. A two-sided P value < 0.05 was considered statistically significant. The data are presented as the mean ± SD for a minimum of three independent experiments unless otherwise indicated.

Materials availability

Plasmids and sequences generated in this study are available from the corresponding author upon reasonable request.

Data availability

The RNA-seq data generated in this study have been deposited in the Genome Sequence Archive (GSA) database under accession code PRJCA041856 (https://bigd.big.ac.cn/gsa-human/browse/HRA018178). The targeted sequencing data of BRCA1/2 have been deposited in the GSA database under accession code PRJCA042581 (https://bigd.big.ac.cn/gsa-human/browse/HRA012188). The mass spectrometry proteomics data have been deposited in the iProX partner repository under accession code PXD065248 (https://www.iprox.cn//page/SCV017.html?query=PXD065248). Data from the FUSCCTNBC cohort are available in The National Omics Data Encyclopedia (NODE) under accession code OEP000155 (http://www.biosino.org/node/project/detail/OEP000155). The I-SPY2 trial data analyzed in this study are available in the GEO database under accession code GSE194040 (https://www.ncbi.nlm.nih.gov/geo/query/acc.cgi?acc=GSE194040). The TCGA datasets analyzed during the current study are available through the cBioPortal website (www.cbioportal.org/). Source data are provided with this paper. The remaining data are available within the Article, Supplementary Information or Source Data file.

References

1 Bianchini, G., De Angelis, C., Licata, L. & Gianni, L. Treatment landscape of triple-negative breast cancer - expanded options, evolving needs. *Nature reviews. Clinical oncology* **19** (2022). https://doi.org/10.1038/s41571-021-00565-2

2 Bianchini, G., Balko, J. M., Mayer, I. A., Sanders, M. E. & Gianni, L. Triple-negative breast cancer: challenges and opportunities of a heterogeneous disease. *Nat Rev Clin Oncol* **13**, 674–690 (2016). https://doi.org/10.1038/nrclinonc.2016.66

3 Papadimitriou, M., Mountzios, G. & Papadimitriou, C. A. The role of PARP inhibition in triple-negative breast cancer: Unraveling the wide spectrum of synthetic lethality. *Cancer Treat Rev* **67**, 34–44 (2018). https://doi.org/10.1016/j.ctrv.2018.04.010

4 Lord, C. J. & Ashworth, A. PARP inhibitors: Synthetic lethality in the clinic. *Science (New York, N.Y.)* **355**, 1152–1158 (2017). https://doi.org/10.1126/science.aam7344

5 Robson, M. *et al.* Olaparib for Metastatic Breast Cancer in Patients with a Germline BRCA Mutation. *N Engl J Med* **377**, 523–533 (2017). https://doi.org/10.1056/NEJMoa1706450

6 Litton, J. K. *et al.* Talazoparib in Patients with Advanced Breast Cancer and a Germline BRCA Mutation. *N Engl J Med* **379**, 753–763 (2018). https://doi.org/10.1056/NEJMoa1802905

7 Geyer, C. E., Jr. *et al.* Overall survival in the OlympiA phase III trial of adjuvant olaparib in patients with germline pathogenic variants in BRCA1/2 and high-risk, early breast cancer. *Ann Oncol* **33**, 1250–1268 (2022). https://doi.org/10.1016/j.annonc.2022.09.159

8 Blackford, A. N. & Jackson, S. P. ATM, ATR, and DNA-PK: The Trinity at the Heart of the

DNA Damage Response. *Mol Cell* **66**, 801–817 (2017). https://doi.org/10.1016/j.molcel.2017.05.015

9 Min, S., Ji, J. H., Heo, Y. & Cho, H. Transcriptional regulation and chromatin dynamics at DNA double-strand breaks. *Exp Mol Med* **54**, 1705–1712 (2022). https://doi.org/10.1038/s12276-022-00862-5

10 Matthews, H. K., Bertoli, C. & de Bruin, R. A. M. Cell cycle control in cancer. *Nat Rev Mol Cell Biol* **23**, 74–88 (2022). https://doi.org/10.1038/s41580-021-00404-3

11 O'Connor, M. J. Targeting the DNA Damage Response in Cancer. *Mol Cell* **60**, 547–560 (2015). https://doi.org/10.1016/j.molcel.2015.10.040

12 Chang, H. H. Y., Pannunzio, N. R., Adachi, N. & Lieber, M. R. Non-homologous DNA end joining and alternative pathways to double-strand break repair. *Nat Rev Mol Cell Biol* **18**, 495–506 (2017). https://doi.org/10.1038/nrm.2017.48

13 Piazza, A. & Heyer, W. D. Homologous Recombination and the Formation of Complex Genomic Rearrangements. *Trends Cell Biol* **29**, 135–149 (2019). https://doi.org/10.1016/j.tcb.2018.10.006

14 Dias, M. P., Moser, S. C., Ganesan, S. & Jonkers, J. Understanding and overcoming resistance to PARP inhibitors in cancer therapy. *Nat Rev Clin Oncol* **18**, 773–791 (2021). https://doi.org/10.1038/s41571-021-00532-x

15 Cassandri, M. *et al.* Zinc-finger proteins in health and disease. *Cell Death Discov* **3**, 17071 (2017). https://doi.org/10.1038/cddiscovery.2017.71

16 Singh, J. K. & van Attikum, H. DNA double-strand break repair: Putting zinc fingers on the sore spot. *Semin Cell Dev Biol* **113**, 65–74 (2021). https://doi.org/10.1016/j.semcdb.2020.09.003

17 Silva, F. P., Hamamoto, R., Furukawa, Y. & Nakamura, Y. TIPUH1 encodes a novel KRAB zinc-finger protein highly expressed in human hepatocellular carcinomas. *Oncogene* **25**, 5063–5070 (2006).

18 Shigematsu, S. *et al.* ZNF689 suppresses apoptosis of hepatocellular carcinoma cells through the down-regulation of Bcl-2 family members. *Exp Cell Res* **317**, 1851–1859 (2011). https://doi.org/10.1016/j.yexcr.2011.05.012

19 Jiang, H. *et al.* MiRNA-339 targets and regulates ZNF689 to inhibit the proliferation and invasion of gastric cancer cells. *Transl Cancer Res* **10**, 3516–3526 (2021). https://doi.org/10.21037/tcr-21-994

20 Ge, L. P. *et al.* ZNF689 deficiency promotes intratumor heterogeneity and immunotherapy resistance in triple-negative breast cancer. *Cell Res* **34**, 58–75 (2024). https://doi.org/10.1038/s41422-023-00909-w

21 Kinner, A., Wu, W., Staudt, C. & Iliakis, G. Gamma-H2AX in recognition and signaling of DNA double-strand breaks in the context of chromatin. *Nucleic acids research* **36**, 5678–5694 (2008). https://doi.org/10.1093/nar/gkn550

22 Chen, G. *et al.* ZNF830 mediates cancer chemoresistance through promoting homologous-recombination repair. *Nucleic acids research* **46**, 1266–1279 (2018).

https://doi.org/10.1093/nar/gkx1258

23 Lee, J. H. *et al.* ID3 regulates the MDC1-mediated DNA damage response in order to maintain genome stability. *Nat Commun* **8**, 903 (2017). https://doi.org/10.1038/s41467-017-01051-z

24 Corrales-Guerrero, S. *et al.* Inhibition of RRM2 radiosensitizes glioblastoma and uncovers synthetic lethality in combination with targeting CHK1. *Cancer Lett* **570**, 216308 (2023). https://doi.org/10.1016/j.canlet.2023.216308

25 Efimova, E. V. *et al.* Poly(ADP-ribose) polymerase inhibitor induces accelerated senescence in irradiated breast cancer cells and tumors. *Cancer research* **70**, 6277–6282 (2010). https://doi.org/10.1158/0008-5472.Can-09-4224

26 Chao, T. *et al.* Autophagy restricts mitochondrial DNA damage-induced release of ENDOG (endonuclease G) to regulate genome stability. *Autophagy* **17**, 3444–3460 (2021). https://doi.org/10.1080/15548627.2021.1874209

27 Pilié, P. G., Tang, C., Mills, G. B. & Yap, T. A. State-of-the-art strategies for targeting the DNA damage response in cancer. *Nat Rev Clin Oncol* **16**, 81–104 (2019). https://doi.org/10.1038/s41571-018-0114-z

28 Jachimowicz, R. D. *et al.* UBQLN4 Represses Homologous Recombination and Is Overexpressed in Aggressive Tumors. *Cell* **176**, 505–519.e522 (2019). https://doi.org/10.1016/j.cell.2018.11.024

29 Muñoz, M. C., Yanez, D. A. & Stark, J. M. An RNF168 fragment defective for focal

accumulation at DNA damage is proficient for inhibition of homologous recombination in BRCA1 deficient cells. *Nucleic acids research* **42**, 7720–7733 (2014). https://doi.org/10.1093/nar/gku421

30 Li, X. & Heyer, W. D. Homologous recombination in DNA repair and DNA damage tolerance. *Cell Res* **18**, 99–113 (2008). https://doi.org/10.1038/cr.2008.1

31 Panier, S. & Boulton, S. J. Double-strand break repair: 53BP1 comes into focus. *Nat Rev Mol Cell Biol* **15**, 7–18 (2014). https://doi.org/10.1038/nrm3719

32 Falck, J., Coates, J. & Jackson, S. P. Conserved modes of recruitment of ATM, ATR and DNA-PKcs to sites of DNA damage. *Nature* **434**, 605–611 (2005). https://doi.org/10.1038/nature03442

33 Ha, G. H. *et al.* Pellino1 regulates reversible ATM activation via NBS1 ubiquitination at DNA double-strand breaks. *Nat Commun* **10**, 1577 (2019). https://doi.org/10.1038/s41467-019-09641-9

34 Lu, C. S. *et al.* The RING finger protein RNF8 ubiquitinates Nbs1 to promote DNA double-strand break repair by homologous recombination. *J Biol Chem* **287**, 43984–43994 (2012). https://doi.org/10.1074/jbc.M112.421545

35 Wu, J. *et al.* Skp2 E3 ligase integrates ATM activation and homologous recombination repair by ubiquitinating NBS1. *Mol Cell* **46**, 351–361 (2012). https://doi.org/10.1016/j.molcel.2012.02.018

36 Bhoj, V. G. & Chen, Z. J. Ubiquitylation in innate and adaptive immunity. *Nature* **458**, 430–

437 (2009). https://doi.org/10.1038/nature07959

37 Yang, W. L. *et al.* The E3 ligase TRAF6 regulates Akt ubiquitination and activation. *Science (New York, N.Y.)* **325**, 1134–1138 (2009). https://doi.org/10.1126/science.1175065

38 Sachs, N. *et al.* A Living Biobank of Breast Cancer Organoids Captures Disease Heterogeneity. *Cell* **172**, 373–386.e310 (2018). https://doi.org/10.1016/j.cell.2017.11.010

39 Yang, L. *et al.* Repression of BET activity sensitizes homologous recombination-proficient cancers to PARP inhibition. *Sci Transl Med* **9** (2017). https://doi.org/10.1126/scitranslmed.aal1645

40 Loibl, S. *et al.* Addition of the PARP inhibitor veliparib plus carboplatin or carboplatin alone to standard neoadjuvant chemotherapy in triple-negative breast cancer (BrighTNess): a randomised, phase 3 trial. *Lancet Oncol* **19**, 497–509 (2018). https://doi.org/10.1016/s1470-2045(18)30111-6

41 Rodler, E. *et al.* Cisplatin with veliparib or placebo in metastatic triple-negative breast cancer and BRCA mutation-associated breast cancer (S1416): a randomised, double-blind, placebo-controlled, phase 2 trial. *Lancet Oncol* **24**, 162–174 (2023). https://doi.org/10.1016/s1470-2045(22)00739-2

42 Telli, M. L. *et al.* Homologous Recombination Deficiency (HRD) Score Predicts Response to Platinum-Containing Neoadjuvant Chemotherapy in Patients with Triple-Negative Breast Cancer. *Clin Cancer Res* **22**, 3764–3773 (2016). https://doi.org/10.1158/1078-0432.Ccr-15-2477

43 Chopra, N. *et al.* Homologous recombination DNA repair deficiency and PARP inhibition

activity in primary triple negative breast cancer. *Nat Commun* **11**, 2662 (2020). https://doi.org/10.1038/s41467-020-16142-7

44 Wolf, D. M. *et al.* Redefining breast cancer subtypes to guide treatment prioritization and maximize response: Predictive biomarkers across 10 cancer therapies. *Cancer Cell* **40**, 609–623.e606 (2022). https://doi.org/10.1016/j.ccell.2022.05.005

45 Jiao, S. *et al.* PARP Inhibitor Upregulates PD-L1 Expression and Enhances Cancer-Associated Immunosuppression. *Clin Cancer Res* **23**, 3711–3720 (2017). https://doi.org/10.1158/1078-0432.Ccr-16-3215

46 Hopfner, K. P. & Hornung, V. Molecular mechanisms and cellular functions of cGAS-STING signalling. *Nat Rev Mol Cell Biol* **21**, 501–521 (2020). https://doi.org/10.1038/s41580-020-0244-x

47 Pantelidou, C. *et al.* PARP Inhibitor Efficacy Depends on CD8(+) T-cell Recruitment via Intratumoral STING Pathway Activation in BRCA-Deficient Models of Triple-Negative Breast Cancer. *Cancer Discov* **9**, 722–737 (2019). https://doi.org/10.1158/2159-8290.Cd-18-1218

48 Voabil, P. *et al.* An ex vivo tumor fragment platform to dissect response to PD-1 blockade in cancer. *Nat Med* **27**, 1250–1261 (2021). https://doi.org/10.1038/s41591-021-01398-3

49 Scully, R. & Livingston, D. M. In search of the tumour-suppressor functions of BRCA1 and BRCA2. *Nature* **408**, 429–432 (2000). https://doi.org/10.1038/35044000

50 Tung, N. *et al.* Frequency of Germline Mutations in 25 Cancer Susceptibility Genes in a Sequential Series of Patients With Breast Cancer. *J Clin Oncol* **34**, 1460–1468 (2016).

https://doi.org/10.1200/jco.2015.65.0747

51 Hopkins, J. L., Lan, L. & Zou, L. DNA repair defects in cancer and therapeutic opportunities. *Genes Dev* **36**, 278–293 (2022). https://doi.org/10.1101/gad.349431.122

52 Yi, P. S., Wu, B., Deng, D. W., Zhang, G. N. & Li, J. S. Positive expression of ZNF689 indicates poor prognosis of hepatocellular carcinoma. *Oncol Lett* **16**, 5122–5130 (2018). https://doi.org/10.3892/ol.2018.9295

53 Zeng, H. *et al.* MicroRNA-339 inhibits human hepatocellular carcinoma proliferation and invasion via targeting ZNF689. *Drug Des Devel Ther* **13**, 435–445 (2019). https://doi.org/10.2147/dddt.S186352

54 Yu, Z., Zhao, S., Wang, L., Wang, J. & Zhou, J. miRNA-339-5p Plays an Important Role in Invasion and Migration of Pancreatic Cancer Cells. *Med Sci Monit* **25**, 7509–7517 (2019). https://doi.org/10.12659/msm.917038

55 Jin, M. H. & Oh, D. Y. ATM in DNA repair in cancer. *Pharmacol Ther* **203**, 107391 (2019). https://doi.org/10.1016/j.pharmthera.2019.07.002

56 Zhang, Y., Zhou, J. & Lim, C. U. The role of NBS1 in DNA double strand break repair, telomere stability, and cell cycle checkpoint control. *Cell Res* **16**, 45–54 (2006). https://doi.org/10.1038/sj.cr.7310007

57 Syed, A. & Tainer, J. A. The MRE11-RAD50-NBS1 Complex Conducts the Orchestration of Damage Signaling and Outcomes to Stress in DNA Replication and Repair. *Annu Rev Biochem* **87**, 263–294 (2018). https://doi.org/10.1146/annurev-biochem-062917-012415

58 Bian, L., Meng, Y., Zhang, M. & Li, D. MRE11-RAD50-NBS1 complex alterations and DNA damage response: implications for cancer treatment. *Mol Cancer* **18**, 169 (2019). https://doi.org/10.1186/s12943-019-1100-5

59 Cejka, P. & Symington, L. S. DNA End Resection: Mechanism and Control. *Annu Rev Genet* **55**, 285–307 (2021). https://doi.org/10.1146/annurev-genet-071719-020312

60 Stingele, J., Bellelli, R. & Boulton, S. J. Mechanisms of DNA-protein crosslink repair. *Nat Rev Mol Cell Biol* **18**, 563–573 (2017). https://doi.org/10.1038/nrm.2017.56

61 Gupta, S. K. *et al.* Delineation of MGMT Hypermethylation as a Biomarker for Veliparib-Mediated Temozolomide-Sensitizing Therapy of Glioblastoma. *J Natl Cancer Inst* **108** (2016). https://doi.org/10.1093/jnci/djv369

62 Diéras, V. *et al.* Veliparib with carboplatin and paclitaxel in BRCA-mutated advanced breast cancer (BROCADE3): a randomised, double-blind, placebo-controlled, phase 3 trial. *Lancet Oncol* **21**, 1269–1282 (2020). https://doi.org/10.1016/s1470-2045(20)30447-2

63 Govindan, R. *et al.* Veliparib Plus Carboplatin and Paclitaxel Versus Investigator's Choice of Standard Chemotherapy in Patients With Advanced Non-Squamous Non-Small Cell Lung Cancer. *Clin Lung Cancer* **23**, 214–225 (2022). https://doi.org/10.1016/j.cllc.2022.01.005

64 Ray-Coquard, I. *et al.* Olaparib plus Bevacizumab as First-Line Maintenance in Ovarian Cancer. *N Engl J Med* **381**, 2416–2428 (2019). https://doi.org/10.1056/NEJMoa1911361

65 Fugger, K., Hewitt, G., West, S. C. & Boulton, S. J. Tackling PARP inhibitor resistance. *Trends Cancer* **7**, 1102–1118 (2021). https://doi.org/10.1016/j.trecan.2021.08.007

66 Morganti, S. *et al.* PARP Inhibitors for Breast Cancer Treatment: A Review. *JAMA Oncol* **10**, 658–670 (2024). https://doi.org/10.1001/jamaoncol.2023.7322

67 Ding, L. *et al.* PARP Inhibition Elicits STING-Dependent Antitumor Immunity in Brca1-Deficient Ovarian Cancer. *Cell Rep* **25**, 2972–2980.e2975 (2018). https://doi.org/10.1016/j.celrep.2018.11.054

68 Vinayak, S. *et al.* Open-label Clinical Trial of Niraparib Combined With Pembrolizumab for Treatment of Advanced or Metastatic Triple-Negative Breast Cancer. *JAMA Oncol* **5**, 1132–1140 (2019). https://doi.org/10.1001/jamaoncol.2019.1029

69 Domchek, S. M. *et al.* Olaparib and durvalumab in patients with germline BRCA-mutated metastatic breast cancer (MEDIOLA): an open-label, multicentre, phase 1/2, basket study. *Lancet Oncol* **21**, 1155–1164 (2020). https://doi.org/10.1016/s1470-2045(20)30324-7

70 Fanucci, K. A. *et al.* Abstract CT145: Olaparib +/- atezolizumab in patients with BRCA-mutated (BRCAmt) locally advanced unresectable or metastatic (advanced) breast cancer: an open-label, multicenter, randomized phase II trial. *Cancer research* **83**, CT145–CT145 (2023). https://doi.org/10.1158/1538-7445.Am2023-ct145

71 Reiss, K. A. *et al.* Niraparib plus nivolumab or niraparib plus ipilimumab in patients with platinum-sensitive advanced pancreatic cancer: a randomised, phase 1b/2 trial. *Lancet Oncol* **23**, 1009–1020 (2022). https://doi.org/10.1016/s1470-2045(22)00369-2

72 Westin, S. N. *et al.* Durvalumab Plus Carboplatin/Paclitaxel Followed by Maintenance Durvalumab With or Without Olaparib as First-Line Treatment for Advanced Endometrial Cancer:

The Phase III DUO-E Trial. *J Clin Oncol* **42**, 283–299 (2024). https://doi.org/10.1200/jco.23.02132

73 Gunn, A. & Stark, J. M. I-SceI-based assays to examine distinct repair outcomes of mammalian chromosomal double strand breaks. *Methods Mol Biol* **920**, 379–391 (2012). https://doi.org/10.1007/978-1-61779-998-3_27

74 Shevchenko, A., Tomas, H., Havlis, J., Olsen, J. V. & Mann, M. In-gel digestion for mass spectrometric characterization of proteins and proteomes. *Nat Protoc* **1**, 2856–2860 (2006). https://doi.org/10.1038/nprot.2006.468

75 Cox, J. & Mann, M. MaxQuant enables high peptide identification rates, individualized p.p.b.-range mass accuracies and proteome-wide protein quantification. *Nat Biotechnol* **26**, 1367–1372 (2008). https://doi.org/10.1038/nbt.1511

76 Tyanova, S. *et al.* The Perseus computational platform for comprehensive analysis of (prote)omics data. *Nat Methods* **13**, 731–740 (2016). https://doi.org/10.1038/nmeth.3901

77 Sztupinszki, Z. *et al.* Migrating the SNP array-based homologous recombination deficiency measures to next generation sequencing data of breast cancer. *NPJ Breast Cancer* **4**, 16 (2018). https://doi.org/10.1038/s41523-018-0066-6

78 Timms, K. M. *et al.* Association of BRCA1/2 defects with genomic scores predictive of DNA damage repair deficiency among breast cancer subtypes. *Breast Cancer Res* **16**, 475 (2014). https://doi.org/10.1186/s13058-014-0475-x

Acknowledgements

The authors thank all the patients who donated samples for this study.

Funding

This work was supported by grants from the National Natural Science Foundation of China (82272822 to Y.-Z.J., 82403908 to L.-P.G., and 82503783 to S.-Y.W.), the Fundamental and Interdisciplinary Disciplines Breakthrough Plan of the Ministry of Education of China (JYB2025XDXM611 to Y.-Z.J.), the Shuguang Program of Shanghai Education Development Foundation and Shanghai Municipal Education Commission (24SG12 to Y.-Z.J.), the Outstanding Youth Medical Talents of Shanghai (WJWRC202306 to Y.-Z.J.), the Shanghai Municipal Health Commission Excellence Project for Health Industry Research (20244Z0016 to Y.-Z.J.), the HE Research Fellowships from the HE Science Foundation (Y.-Z.J.), and the Shanghai Science and Technology Innovation Action Plan (24YF2705900 to S.-Y.W.). Yi-Zhou Jiang is a SANS Exploration Scholar. Y.-L.X., F.-L.Z., E.-R.L., G.-H.D., Z.-M.S., and M.H.S. declare no relevant funding. The funders had no role in the study design, data collection and analysis, decision to publish, or preparation of the manuscript.

Author Contributions Statement

Y.-Z.J. conceived the project, supervised the study, and acquired funding. L.-P.G. designed and conducted the majority of the experiments, analyzed the data, prepared the figures, acquired

funding, and wrote the manuscript. Y.-L.X. and S.-Y.W. contributed to experiments, data analysis, and visualization. S.-Y.W. also provided funding support. M.H.S. and F.-L.Z. provided technical support and contributed to data interpretation and manuscript discussions. E.-R.L. performed bioinformatics analyses. Z.-M.S. and G.-H.D. provided clinical specimens. All authors reviewed and approved the final manuscript.

Competing Interests Statement

The authors declare no competing interests.

Figure Legends

Fig. 1. ZNF689 loss impairs HR repair activity in TNBC.

a GSEA of differentially expressed pathways in MDA-MB-231 cells transfected with siZNF689 or siCtrl. **b, c** γH2AX levels were assessed by western blot in siZNF689 and siCtrl MDA-MB-231 (**b**) and BT-549 (**c**) cells treated with IR (10 Gy) and collected at the indicated time points. **d** Schematic of the DR-GFP reporter system used to assess HR repair efficiency. **e, f** U2OS DR-GFP (**e**) and MDA-MB-231 DR-GFP (**f**) cells were transfected with siZNF689 or siCtrl, followed by I-SceI transfection. The percentage of GFP-positive cells was quantified by flow cytometry. siBRCA2 served as a positive control. **g** IF analysis of RAD51 foci formation in MDA-MB-231 cells transfected with siCtrl, siZNF689, siBRCA2, or siZNF689 plus BRCA2 OE, following IR (6 Gy). Representative images and quantification of RAD51 foci per cell at 4 h post-IR are shown. Scale bar, 10 μm. **h** Metaphase spread analysis of chromosomal aberrations in MDA-MB-231 cells transfected with siZNF689 or siCtrl, assessed 2 h after IR (10 Gy). Scale bar, 10 μm. Results in **b**, **c** were representative of n = 3 biologically independent experiments. Data in **e**–**h** were presented as mean ± SD of n = 3 biologically independent experiments. For GSEA in **a**, significance was assessed by empirical permutation tests and adjusted for multiple comparisons via false discovery rate (FDR). P values were determined by one-way ANOVA (**e**–**g**) or two-tailed unpaired Student's t-test (**h**). Source data are provided as a Source Data file. HR, homologous recombination; IR, ionizing radiation; NES, normalized enrichment score; OE, overexpression.

Fig. 2. Recruitment of ZNF689 to the DSBs sites depends on the Ser215 phosphorylation by ATM.

a Representative PLA images showing *in situ* co-localization of ZNF689 and γH2AX in MDA-MB-231 cells at 4 h post-irradiation (6 Gy). Scale bar, 5 μm. **b** U2OS DR-GFP cells were transfected with siZNF689 or siCtrl, followed by I-SceI transfection to induce site-specific DNA DSBs. ChIP was performed using anti-MRE11, RAD50, or NBS1 antibodies, and DNA fragments were detected by PCR. Top: schematic overview of the ChIP assay; bottom: representative PCR results. **c** HEK293T cells were exposed to IR (10 Gy) and harvested 1 h later for IP with anti-Flag antibody, followed by western blot analysis of ZNF689 phosphorylation using an anti-phospho-ATM/ATR/DNA-PKcs substrate antibody. **d** Sequence alignment of the conserved SQ/TQ DNA damage-responsive phosphorylation motifs in ZNF689 across species. **e** HEK293T cells were transfected with the indicated Flag-ZNF689 phosphorylation site mutants and treated with IR (10 Gy). ZNF689 phosphorylation was assessed 1 h post-IR by IP with anti-Flag followed by western blot using the phospho-ATM/ATR/DNA-PKcs substrate antibody. **f** MDA-MB-231 cells were transfected with Flag-ZNF689 and pre-treated with ATM (10 μM), ATR (10 μM), or DNA-PKcs (10 μM) inhibitors for 1 h prior to IR (10 Gy). Cells were harvested 1 h post-IR for IP and phosphorylation analysis. **g** MDA-MB-231 cells were transfected with either WT or S215A mutant Flag-ZNF689, with or without siATM, followed by IR (6 Gy). Co-immunostaining of Flag and γH2AX was performed 4 h post-IR to assess recruitment to DSBs. Scale bar, 5 μm. Results in **a-c, e, f** were representative of *n* = 3 biologically independent experiments. Data in **g** was

presented as mean ± SD of *n* = 3 biologically independent experiments. *P* value was determined by one-way ANOVA. Source data are provided as a Source Data file. ChIP, chromatin immunoprecipitation; DSB, double-strand break; IP, immunoprecipitation; IR, ionizing radiation; WT, wild-type.

Fig. 3. ZNF689 directly interacts with NBS1 through its zinc-finger domains.

a Co-IP of endogenous ZNF689 was performed in MDA-MB-231 cells without IR treatment using an anti-ZNF689 antibody, followed by western blot analysis of the indicated HR proteins. **b** Co-IP of endogenous ZNF689 and components of the MRN complex in MDA-MB-231 cells, followed by western blot. **c, d** *In vitro* pull-down assays using recombinant GST-ZNF689 (**c**) and His-NBS1 (**d**), followed by western blot. The arrow indicates the specific band of GST-ZNF689. **e** Representative images (left) and quantification (right) of *in situ* PLA signals of ZNF689 and NBS1 in MDA-MB-231 cells. Cells were treated with IR (6 Gy) and analyzed at 4 h post-irradiation. Scale bar, 5 μm. **f** MDA-MB-231 cells were co-transfected with GFP-ZNF689 and mCherry-NBS1 expression plasmids. At 48 h post-transfection, cells were subjected to laser microirradiation, and recruitment of GFP-ZNF689 and mCherry-NBS1 to laser-induced DNA damage stripes was monitored over time. Scale bar, 5 μm. **g, h** Reciprocal co-IP of endogenous ZNF689 (**g**) and NBS1 (**h**) in MDA-MB-231 cells 1 h after IR (10 Gy). **i** Schematic diagram of Flag-ZNF689 and its deletion mutants. **j** Co-IP was performed in HEK293T cells expressing HA-NBS1 and either WT or mutant Flag-ZNF689 constructs. **k** HR efficiency in U2OS DR-GFP cells transfected with siCtrl or siZNF689, with or without rescue using ZNF689-WT, ZNF689-ZFD, or ZNF689-ΔZFD. Results in **a-d, f-h, j** were representative of n = 3 biologically independent experiments. Data in **e, k** were presented as mean ± SD of n = 3 biologically independent experiments. P values were determined by one-way ANOVA. Source data are provided as a Source Data file. HR, homologous recombination; IP, immunoprecipitation; IR, ionizing radiation;

WT, wild-type; ZFD, zinc-finger domain.

Fig. 4. Phosphorylation-mediated ZNF689 promotes NBS1 ubiquitination through SKP2. **a** *In vivo* ubiquitination assay of NBS1 ubiquitination in HEK293T cells co-transfected with Flag-ZNF689, HA-NBS1, and His-tagged ubiquitin (His-Ub). **b** *In vivo* ubiquitination assay of NBS1 ubiquitination in HEK293T cells with or without ZNF689 knockdown, performed 1 h after IR (10 Gy). **c** *In vivo* ubiquitination assay of K63-linked NBS1 ubiquitination in HEK293T cells transfected with either WT or S215A mutant Flag-ZNF689 and His-Ub, 1 h after IR (10 Gy). **d** *In vivo* ubiquitination assay of NBS1 ubiquitination in HEK293T cells co-transfected with Flag-ZNF689, HA-NBS1, and His-Ub, with or without siSKP2. **e** Co-IP of endogenous ZNF689 and SKP2 in MDA-MB-231 cells, followed by western blot analysis. **f, g** Co-IP assays showing altered interaction between SKP2 and NBS1 in ZNF689-KO MDA-MB-231 cells, using anti-SKP2 (**f**) or anti-NBS1 (**g**) antibodies. **h** IF analysis of SKP2 recruitment to DNA damage sites in ZNF689-KO MDA-MB-231 cells with or without re-expression of WT or S215A ZNF689. Cells were irradiated (6 Gy) and fixed 4 h post-treatment. Quantification of SKP2 foci per cell is shown. Scale bar, 5 μm. Results in **a-g** were representative of n = 3 biologically independent experiments. Data in **h** was presented as mean ± SD of n = 3 biologically independent experiments. P values were determined by one-way ANOVA. Source data are provided as a Source Data file. IP, immunoprecipitation; IR, ionizing radiation; Ub, ubiquitin; WT, wild-type.

Fig. 5. ZNF689-mediated NBS1 ubiquitination stabilizes the MRN complex and promotes ATM activation.

a Co-IP analysis of NBS1 interactions with MRE11 and RAD50 in ZNF689-KO MDA-MB-231 cells at 1 h post-IR (10 Gy). **b** ChIP-PCR analysis showing the recruitment of MRE11, RAD50, and NBS1 to I-SceI-induced DSB sites in the indicated U2OS DR-GFP cells. **c** IF analysis of RPA2 foci formation in the indicated MDA-MB-231 cells at 4 h post-IR (6 Gy). Cells were pretreated with the MRE11 inhibitor mirin (10 μM, 24 h) to evaluate MRN dependency. In rescue experiments, ZNF689-KO cells were transfected with NBS1 WT or K735R prior to IR. Scale bar, 5 μm. **d** Co-IP analysis of the interaction between NBS1 and ATM in ZNF689-KO MDA-MB-231 cells at 1 h post-IR (10 Gy). **e** IF analysis in MDA-MB-231 cells showing p-ATM foci formation after 4h post-IR treatment (6 Gy) in ZNF689 KO cells, with restoration of either NBS1 WT or K735R. Scale bar, 5 μm. **f** IF analysis of the colocalization between NBS1 and p-ATM at 4 h post-IR (6 Gy) in ZNF689-KO cells transfected with either NBS1 WT or K735R mutant. Scale bar, 5 μm. Results in **a, b, d** were representative of $n = 3$ biologically independent experiments. Data in **c, e, f** were presented as mean ± SD of $n = 3$ biologically independent experiments. *P* values were determined by one-way ANOVA. Source data are provided as a Source Data file. ChIP, chromatin immunoprecipitation; IP, immunoprecipitation; IR, ionizing radiation; WT, wild-type.

Fig. 6. ZNF689 loss confers sensitivity to PARPi in TNBC.

a Dose-response curves and half maximal inhibitory concentration (IC50) values of olaparib in MDA-MB-231 cells expressing sgCtrl or sgZNF689. **b** Clonogenic survival assays of MDA-MB-231 cells expressing sgCtrl or sgZNF689 treated with increasing concentrations of olaparib. **c** Western blot analysis of ZNF689 expression in three patient-derived TNBC organoid models. **d, e** Cell viability assays (**d**) and representative bright-field images (**e**) of the three TNBC organoid models treated with 0, 10, or 30 μM olaparib. **f-h** Schematic of the MDA-MB-231 xenograft experiment in NOD/SCID mice. MDA-MB-231 cells expressing sgCtrl or sgZNF689 were implanted into the MFP. Once tumors reached ~100 mm^3, mice were randomized and treated with vehicle or olaparib (50 mg/kg, 5 days/week for 3 weeks) (**f**). Tumor growth curves (**g**) and endpoint tumor weights (**h**) are shown. n = 6 mice per group. **i-k** Schematic of TNBC PDX model generation (**i**). Representative IHC images of ZNF689 expression in two TNBC patients (**j**). Tumor growth curves of TNBC-1 and TNBC-2 PDXs treated with vehicle or olaparib (50 mg/kg, 5 days/week for 4 weeks) (**k**). n = 6 mice per group. **l-n** Schematic of drug treatment design in TNBC-2 PDX model. Mice were treated with vehicle, paclitaxel (20 mg/kg), olaparib (50 mg/kg), or their combination for 4 weeks (**l**). Tumor growth curves (**m**) and endpoint tumor weights (**n**) are shown. n = 6 mice per group. Results in **c, e** were representative of n = 3 biologically independent experiments. Data in **a, b, d** were presented as mean ± SD of n = 3 biologically independent experiments. P values were determined by one-way ANOVA (**a**, **d**, **h**, **n**) or two-way ANOVA (**b**, **g**, **k**, **m**). Source data are provided as a Source Data file. Schematics

in **f**, **i**, and **l** were created in BioRender. Ge, L. (2026) https://BioRender.com/4rsz4kg. PDO, patient-derived organoid; PDX, patient-derived xenograft; TNBC, triple-negative breast cancer.

Fig. 7. PARPi upregulates PD-L1 expression more potently in ZNF689-deficient TNBC via activating the STING pathway.

a, b Comparison of HRD scores in the FUSCCTNBC cohort (**a**) and the PARPi response signature in the I-SPY2 trial (**b**) between ZNF689-high and -low groups, stratified by median mRNA expression. **c** IHC assessment of ZNF689 in tumors from PARPi-treated TNBC responders (*n* = 3) versus non-responders (*n* = 4). Created in BioRender. Ge, L. (2026) https://BioRender.com/4rsz4kg. **d-f** Surface PD-L1 (**d**), PD-L1 mRNA (**e**), and total PD-L1 protein (**f**) levels in MDA-MB-231 sgCtrl or sgZNF689 cells treated with olaparib (10 μM, 24 h). **g** IHC of PD-L1 in xenograft tumors derived from MDA-MB-231 sgCtrl or sgZNF689 cells treated with olaparib (50 mg/kg). *n* = 6 mice per group. Scale bar, 50 μm. **h, i** Intracellular cGAMP levels (**h**) and western blot of STING pathway activation (**i**) in cells treated as in **d**. **j** IF images of cGAS/DAPI staining (left), quantification of micronucleated cells (middle), and cGAS-positive micronuclei (right) in indicated cells. Scale bar, 10 μm. **k, l** RT-qPCR of IFNB, CCL5, and CXCL10 mRNA (**k**) and ELISA of secreted IFN-β (**l**) from cells treated as in **d**. Results in **f, i** were representative of *n* = 3 biologically independent experiments. Data in **d, e, h, j-l** were presented as mean ± SD of *n* = 3 biologically independent experiments. For violin plots (**a, b**), the shape represents data distribution. For embedded box plots, the center line represents the median, bounds show the 25th and 75th percentiles (interquartile range, IQR), and whiskers extend to minimum and maximum values within 1.5 × IQR. *P* values were determined by two-sided Wilcoxon tests (**a**, **b**), two-tailed unpaired Student's *t*-test (**c**) and one-way ANOVA (**d**, **e**,

g, **h**, **j**, **k**, **l**). Source data are provided as a Source Data file. FFPE, formalin-fixed, paraffin-embedded; HRD, homologous recombination deficiency; PARPi, PARP inhibitor.

Fig. 8. PARPi enhances the therapeutic efficacy of PD-L1 blockade in ZNF689-deficient TNBC.

a-d Schematic of the 4T1 mouse xenograft model. 4T1 sgZNF689 cells were implanted into the MFP of BALB/c mice. Once tumors reached ~100 mm^3, mice were randomized into four groups and treated for 2 weeks with either IgG control (100 μg, every 3 days), anti-PD-L1 antibody (αPD-L1, 100 μg, every 3 days), olaparib (50 mg/kg, 5 days per week), or the combination of αPD-L1 and olaparib (**a**). Tumor growth curves (**b**), endpoint tumor weights (**c**), and flow cytometry analysis of tumor-infiltrating $CD4^+$ T cells, $CD8^+$ T cells, $GZMB^+$ $CD8^+$ T cells, and IFN-γ^+ $CD8^+$ T cells (**d**) are shown. *n* = 6 mice per group. **e-g** Overview of the PDTF platform (**e**). Delta values of T cell activation markers (ICOS, CD137, CD25) (**f**) and cytotoxic markers (IFN-γ, TNF-α) (**g**) between αPD-L1 monotherapy and αPD-L1 plus olaparib combination were compared in tumors with low and high ZNF689 expression. *n* = 5 per group. **h** Schematic model summarizing the proposed mechanism of this study. Data were presented as mean ± SD. *P* values were determined by two-way ANOVA (**b**) or one-way ANOVA (**c**, **d**) and two-tailed unpaired Student's *t*-test (**f**, **g**). Source data are provided as a Source Data file. Schematics in **a**, **e**, and **h** were created in BioRender. Ge, L. (2026) https://BioRender.com/4rsz4kg. HR, homologous recombination; PARPi, PARP inhibitor; TNBC, triple-negative breast cancer.

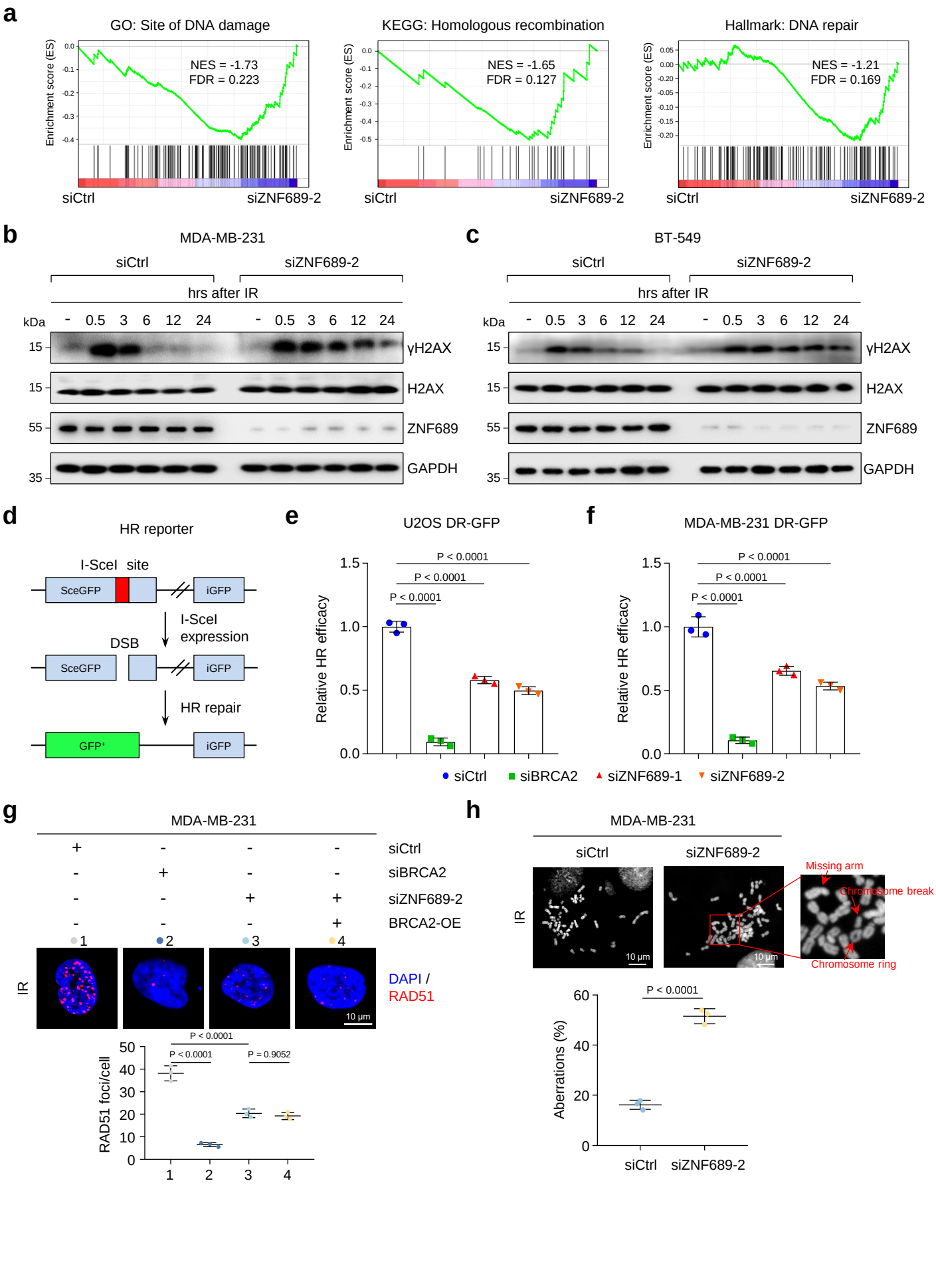
a
GO: Site of DNA damage
NES = -1.73
FDR = 0.223
KEGG: Homologous recombination
NES = -1.65
FDR = 0.127
Hallmark: DNA repair
NES = -1.21
FDR = 0.169
Enrichment score (ES)
siCtrl
siZNF689-2
b
MDA-MB-231
c
BT-549
siCtrl
siZNF689-2
hrs after IR
kDa
- 0.5 3 6 12 24 - 0.5 3 6 12 24
γH2AX
H2AX
ZNF689
GAPDH
d
HR reporter
I-SceI site
SceGFP
iGFP
I-SceI expression
DSB
HR repair
GFP+
e
U2OS DR-GFP
f
MDA-MB-231 DR-GFP
Relative HR efficacy
P < 0.0001
siCtrl
siBRCA2
siZNF689-1
siZNF689-2
g
MDA-MB-231
siCtrl
siBRCA2
siZNF689-2
BRCA2-OE
IR
DAPI / RAD51
10 μm
RAD51 foci/cell
P = 0.9052
h
MDA-MB-231
Missing arm
Chromosome break
Chromosome ring
Aberrations (%)

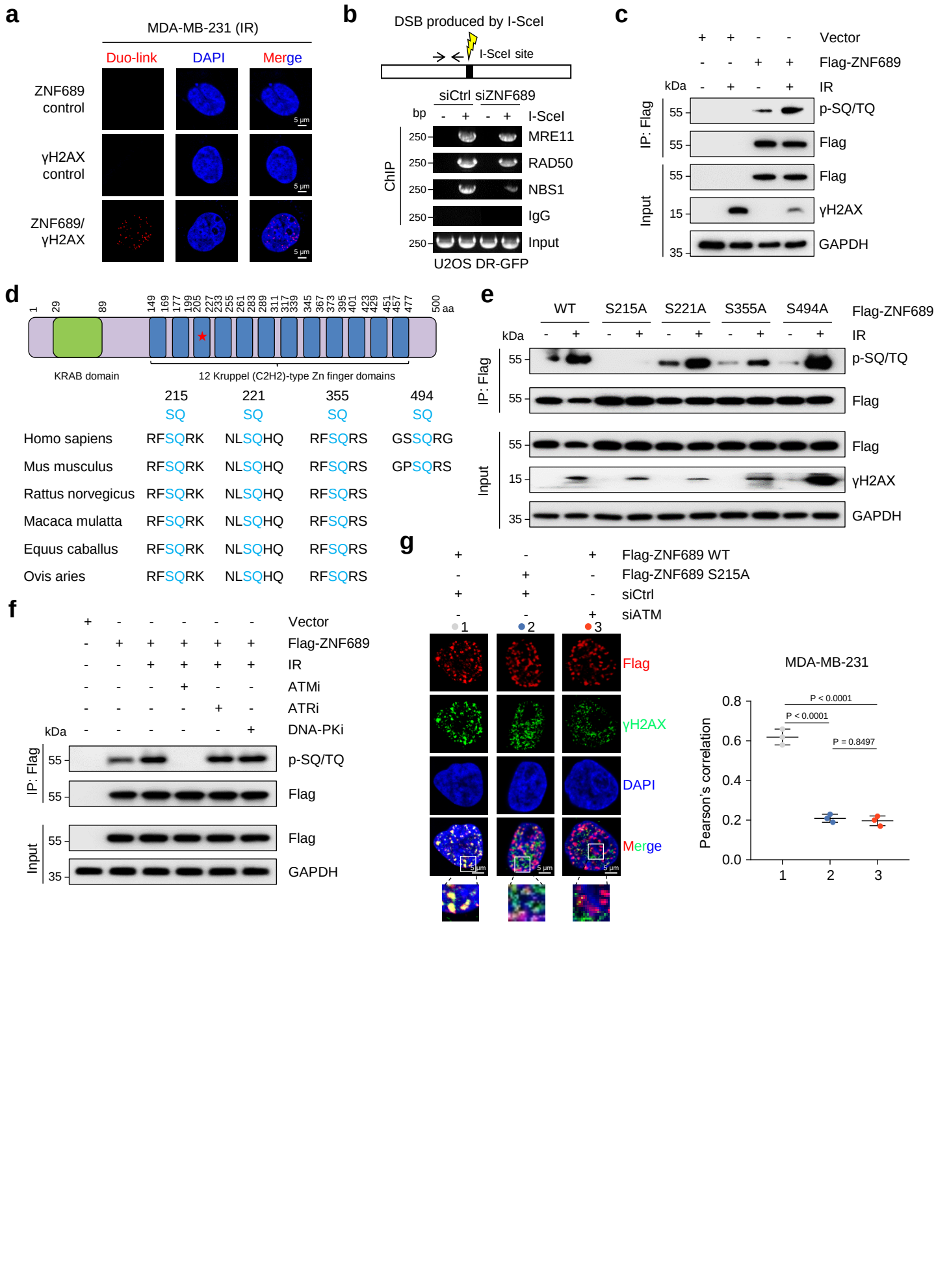
a
MDA-MB-231 (IR)
Duo-link
DAPI
Merge
ZNF689 control
γH2AX control
ZNF689/ γH2AX
5 μm
b
DSB produced by I-SceI
I-SceI site
siCtrl siZNF689
bp - + - +
I-SceI
ChIP
250 MRE11
250 RAD50
250 NBS1
250 IgG
250 Input
U2OS DR-GFP
c
+ + - - Vector
- - + + Flag-ZNF689
kDa - + - + IR
IP: Flag
55 p-SQ/TQ
55 Flag
Input
55 Flag
15 γH2AX
35 GAPDH
d
1 29 89 149 169 177 199 205 227 233 255 261 283 289 311 317 339 345 367 373 395 401 423 429 451 457 477 500 aa
KRAB domain
12 Kruppel (C2H2)-type Zn finger domains
215 SQ
221 SQ
355 SQ
494 SQ
Homo sapiens RFSQRK NLSQHQ RFSQRS GSSQRG
Mus musculus RFSQRK NLSQHQ RFSQRS GPSQRS
Rattus norvegicus RFSQRK NLSQHQ RFSQRS
Macaca mulatta RFSQRK NLSQHQ RFSQRS
Equus caballus RFSQRK NLSQHQ RFSQRS
Ovis aries RFSQRK NLSQHQ RFSQRS
e
WT S215A S221A S355A S494A Flag-ZNF689
kDa - + - + - + - + - + IR
IP: Flag
55 p-SQ/TQ
55 Flag
Input
55 Flag
15 γH2AX
35 GAPDH
f
+ - - - - - Vector
- + + + + + Flag-ZNF689
- - + + + + IR
- - - + - - ATMi
- - - - + - ATRi
kDa - - - - - + DNA-PKi
IP: Flag
55 p-SQ/TQ
55 Flag
Input
55 Flag
35 GAPDH
g
+ - + Flag-ZNF689 WT
- + - Flag-ZNF689 S215A
+ + - siCtrl
- - + siATM
1 2 3
Flag
γH2AX
DAPI
Merge
5 μm
MDA-MB-231
Pearson's correlation
0.8
0.6
0.4
0.2
0.0
P < 0.0001
P < 0.0001
P = 0.8497
1 2 3

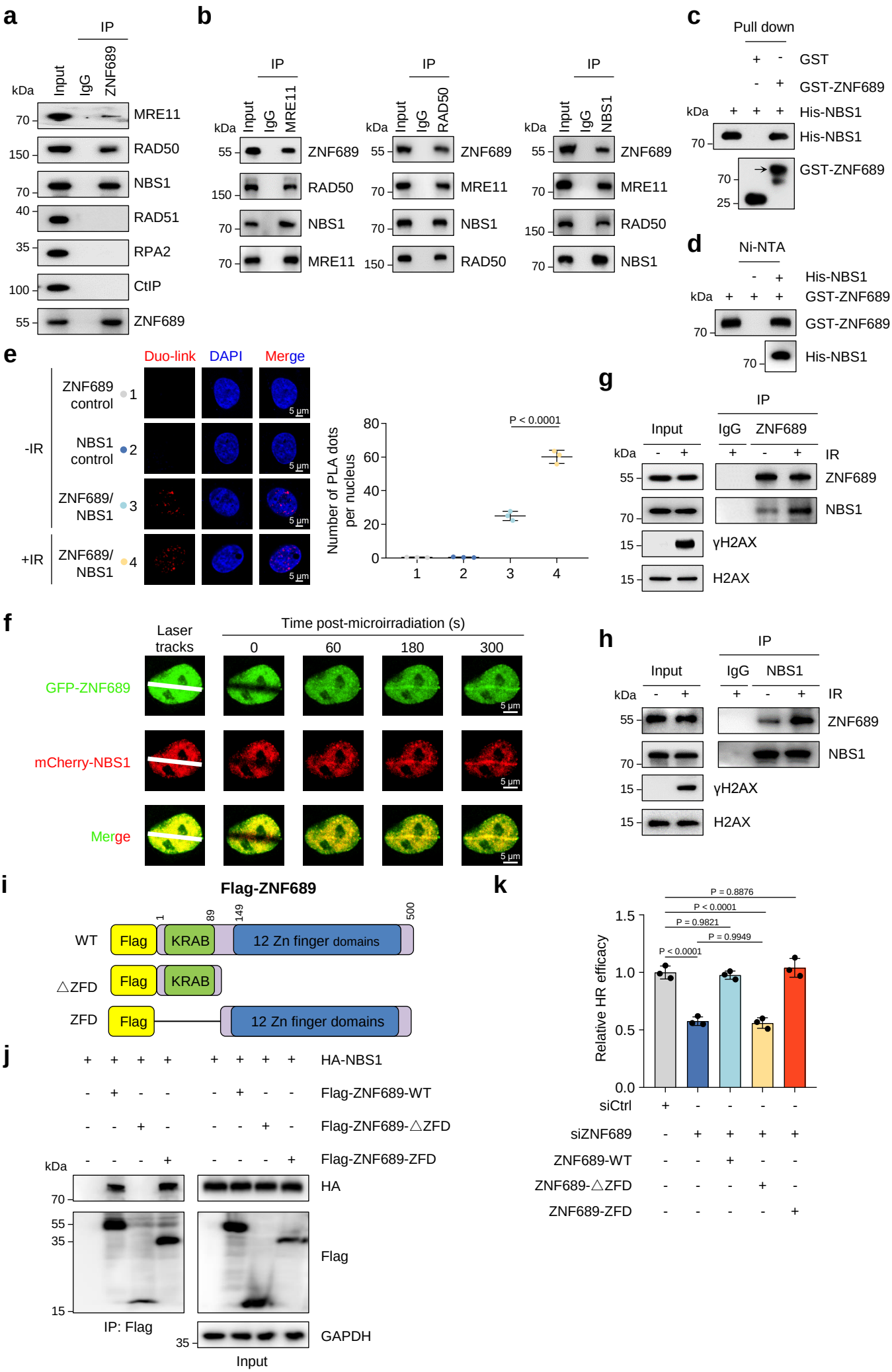
a
IP
Input
IgG
ZNF689
kDa
70
MRE11
150
RAD50
70
NBS1
40
RAD51
35
RPA2
100
CtIP
55
ZNF689
b
IP
Input
IgG
MRE11
kDa
55
ZNF689
150
RAD50
70
NBS1
70
MRE11
IP
Input
IgG
RAD50
kDa
55
ZNF689
70
MRE11
70
NBS1
150
RAD50
IP
Input
IgG
NBS1
kDa
55
ZNF689
70
MRE11
150
RAD50
70
NBS1
c
Pull down
+ - GST
- + GST-ZNF689
kDa + + + His-NBS1
70
His-NBS1
70
25
GST-ZNF689
d
Ni-NTA
- + His-NBS1
kDa + + + GST-ZNF689
70
GST-ZNF689
70
His-NBS1
e
Duo-link
DAPI
Merge
-IR
ZNF689 control
1
NBS1 control
2
ZNF689/ NBS1
3
+IR
ZNF689/ NBS1
4
5 μm
Number of PLA dots per nucleus
P < 0.0001
80
60
40
20
0
1
2
3
4
g
IP
Input
IgG
ZNF689
kDa
- +
+ - +
IR
55
ZNF689
70
NBS1
15
γH2AX
15
H2AX
f
Laser tracks
Time post-microirradiation (s)
0
60
180
300
GFP-ZNF689
mCherry-NBS1
Merge
5 μm
h
IP
Input
IgG
NBS1
kDa
- +
+ - +
IR
55
ZNF689
70
NBS1
15
γH2AX
15
H2AX
i
Flag-ZNF689
1
89
149
500
WT
Flag
KRAB
12 Zn finger domains
△ZFD
Flag
KRAB
ZFD
Flag
12 Zn finger domains
k
P = 0.8876
P < 0.0001
P = 0.9821
P = 0.9949
P < 0.0001
Relative HR efficacy
1.5
1.0
0.5
0.0
siCtrl + - - - -
siZNF689 - + + + +
ZNF689-WT - - + - -
ZNF689-△ZFD - - - + -
ZNF689-ZFD - - - - +
j
HA-NBS1 + + + + + + + +
Flag-ZNF689-WT - + - - - + - -
Flag-ZNF689-△ZFD - - + - - - + -
Flag-ZNF689-ZFD - - - + - - - +
kDa
70
HA
55
35
15
Flag
IP: Flag
35
GAPDH
Input

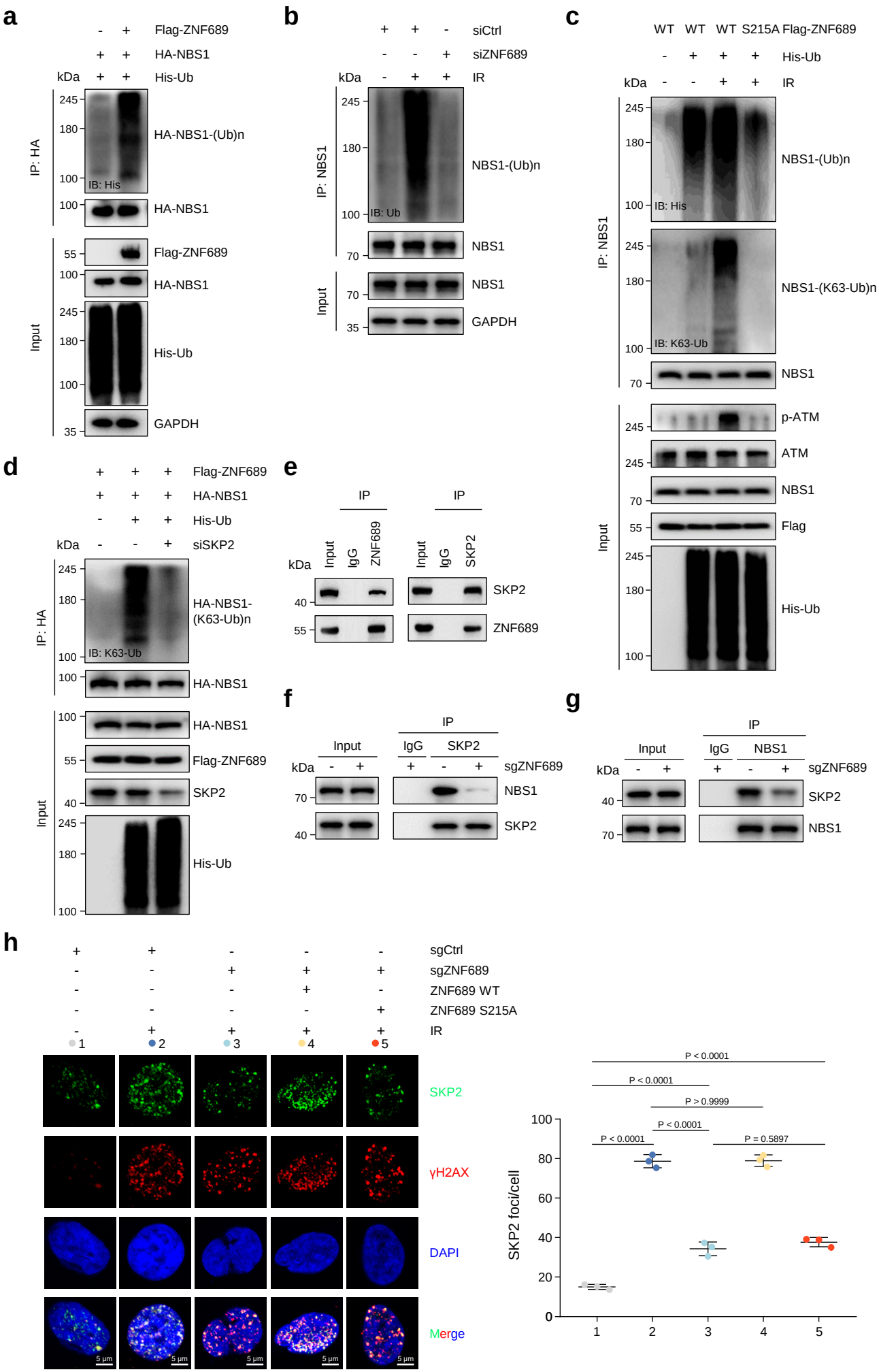
a
Flag-ZNF689
HA-NBS1
His-Ub
kDa
IP: HA
HA-NBS1-(Ub)n
IB: His
HA-NBS1
Input
Flag-ZNF689
HA-NBS1
His-Ub
GAPDH
b
siCtrl
siZNF689
IR
IP: NBS1
NBS1-(Ub)n
IB: Ub
NBS1
Input
NBS1
GAPDH
c
WT WT WT S215A Flag-ZNF689
His-Ub
IR
IP: NBS1
NBS1-(Ub)n
IB: His
NBS1-(K63-Ub)n
IB: K63-Ub
NBS1
Input
p-ATM
ATM
NBS1
Flag
His-Ub
d
Flag-ZNF689
HA-NBS1
His-Ub
siSKP2
IP: HA
HA-NBS1-(K63-Ub)n
IB: K63-Ub
HA-NBS1
Input
HA-NBS1
Flag-ZNF689
SKP2
His-Ub
e
IP
Input
IgG
ZNF689
SKP2
f
IP
Input
IgG
SKP2
sgZNF689
NBS1
g
IP
Input
IgG
NBS1
sgZNF689
SKP2
h
sgCtrl
sgZNF689
ZNF689 WT
ZNF689 S215A
IR
SKP2
γH2AX
DAPI
Merge
5 μm
SKP2 foci/cell
P < 0.0001
P < 0.0001
P > 0.9999
P < 0.0001
P < 0.0001
P = 0.5897

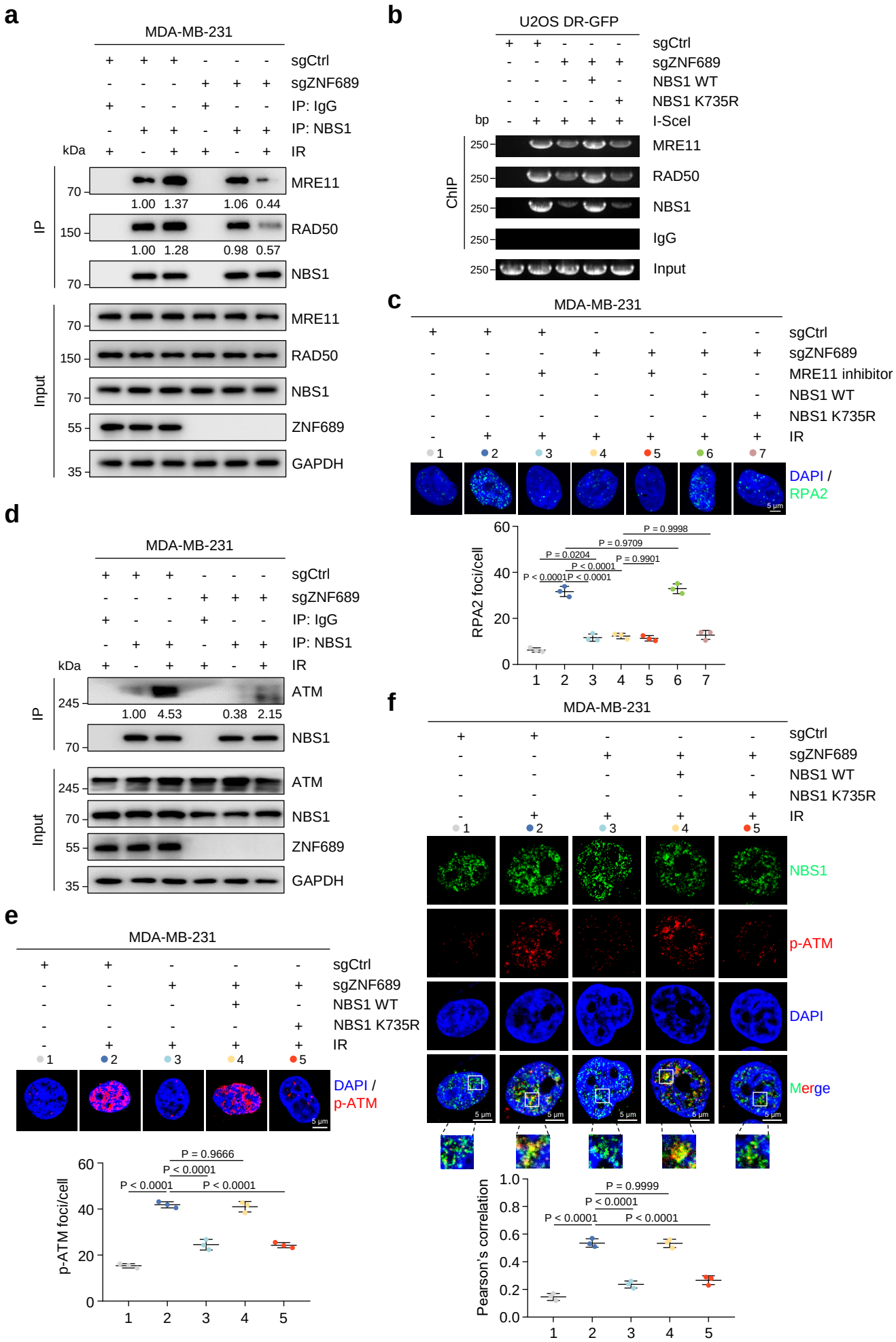
a
MDA-MB-231
sgCtrl
sgZNF689
IP: IgG
IP: NBS1
IR
kDa
IP
MRE11
RAD50
NBS1
Input
MRE11
RAD50
NBS1
ZNF689
GAPDH
1.00 1.37 1.06 0.44
1.00 1.28 0.98 0.57
b
U2OS DR-GFP
sgCtrl
sgZNF689
NBS1 WT
NBS1 K735R
I-SceI
bp
ChIP
MRE11
RAD50
NBS1
IgG
Input
c
MDA-MB-231
MRE11 inhibitor
DAPI / RPA2
RPA2 foci/cell
P = 0.9998
P = 0.9709
P = 0.0204
P = 0.9901
P < 0.0001
P < 0.0001P < 0.0001
d
MDA-MB-231
ATM
1.00 4.53 0.38 2.15
e
MDA-MB-231
DAPI / p-ATM
p-ATM foci/cell
P = 0.9666
P < 0.0001
P < 0.0001
P < 0.0001
f
MDA-MB-231
NBS1
p-ATM
DAPI
Merge
Pearson's correlation
P = 0.9999
P < 0.0001
P < 0.0001
P < 0.0001

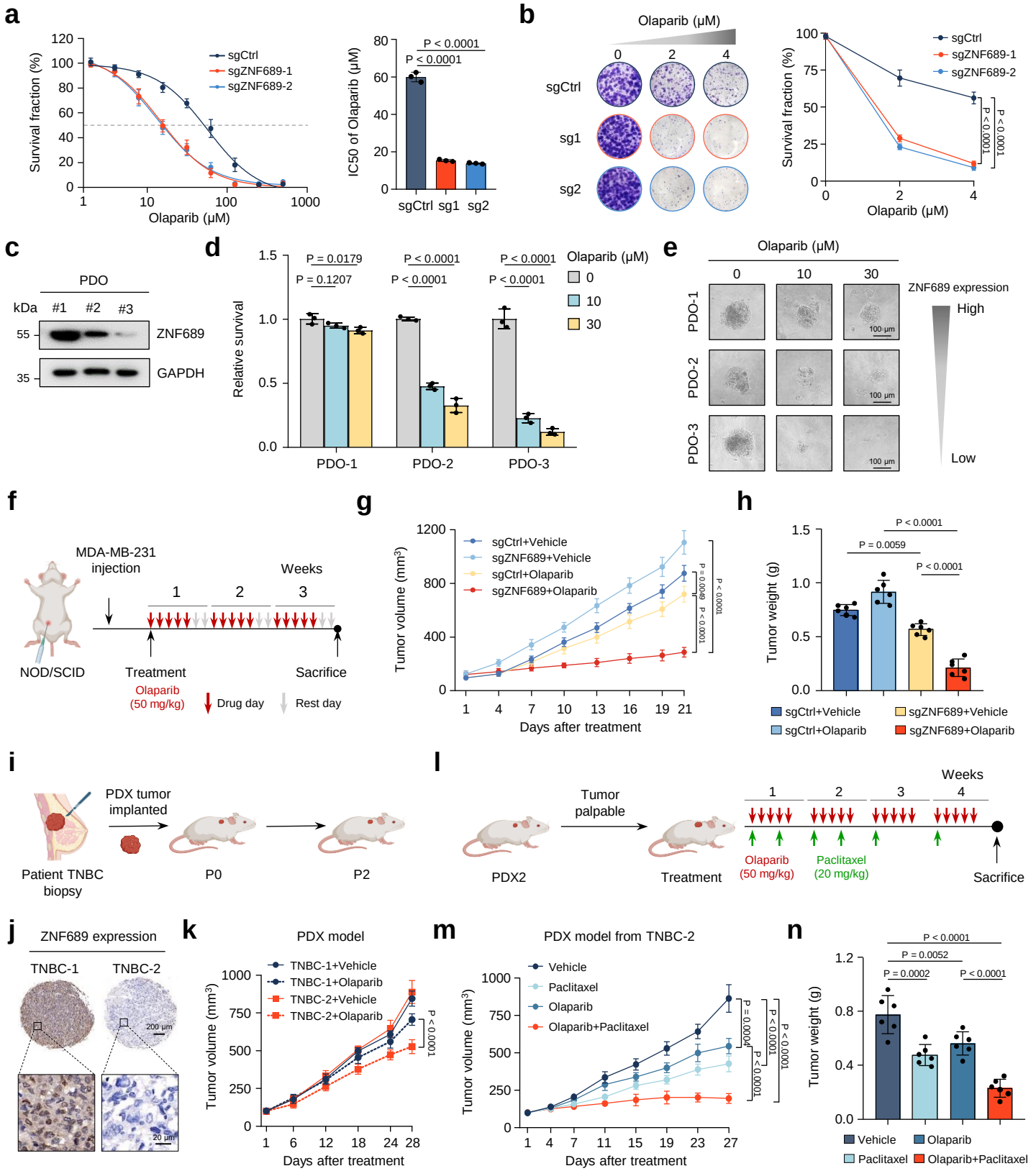
a
Survival fraction (%)
sgCtrl
sgZNF689-1
sgZNF689-2
Olaparib (μM)
IC50 of Olaparib (μM)
P < 0.0001
P < 0.0001
sgCtrl sg1 sg2
b
Olaparib (μM)
0 2 4
sgCtrl
sg1
sg2
Survival fraction (%)
sgCtrl
sgZNF689-1
sgZNF689-2
P < 0.0001
P < 0.0001
Olaparib (μM)
c
PDO
kDa #1 #2 #3
55
ZNF689
35
GAPDH
d
Relative survival
P = 0.0179
P = 0.1207
P < 0.0001
P < 0.0001
P < 0.0001
P < 0.0001
Olaparib (μM)
0
10
30
PDO-1
PDO-2
PDO-3
e
Olaparib (μM)
0 10 30
PDO-1
PDO-2
PDO-3
100 μm
ZNF689 expression
High
Low
f
MDA-MB-231 injection
Weeks
1 2 3
NOD/SCID
Treatment
Olaparib (50 mg/kg)
Drug day
Rest day
Sacrifice
g
Tumor volume (mm3)
sgCtrl+Vehicle
sgZNF689+Vehicle
sgCtrl+Olaparib
sgZNF689+Olaparib
P = 0.0049
P < 0.0001
P < 0.0001
Days after treatment
h
Tumor weight (g)
P < 0.0001
P = 0.0059
P < 0.0001
sgCtrl+Vehicle
sgZNF689+Vehicle
sgCtrl+Olaparib
sgZNF689+Olaparib
i
PDX tumor implanted
Patient TNBC biopsy
P0
P2
l
Tumor palpable
PDX2
Treatment
Weeks
1 2 3 4
Olaparib (50 mg/kg)
Paclitaxel (20 mg/kg)
Sacrifice
j
ZNF689 expression
TNBC-1
TNBC-2
200 μm
20 μm
k
PDX model
TNBC-1+Vehicle
TNBC-1+Olaparib
TNBC-2+Vehicle
TNBC-2+Olaparib
Tumor volume (mm3)
P < 0.0001
Days after treatment
m
PDX model from TNBC-2
Vehicle
Paclitaxel
Olaparib
Olaparib+Paclitaxel
Tumor volume (mm3)
P = 0.0004
P < 0.0001
P < 0.0001
Days after treatment
n
Tumor weight (g)
P < 0.0001
P = 0.0052
P = 0.0002
P < 0.0001
Vehicle
Olaparib
Paclitaxel
Olaparib+Paclitaxel

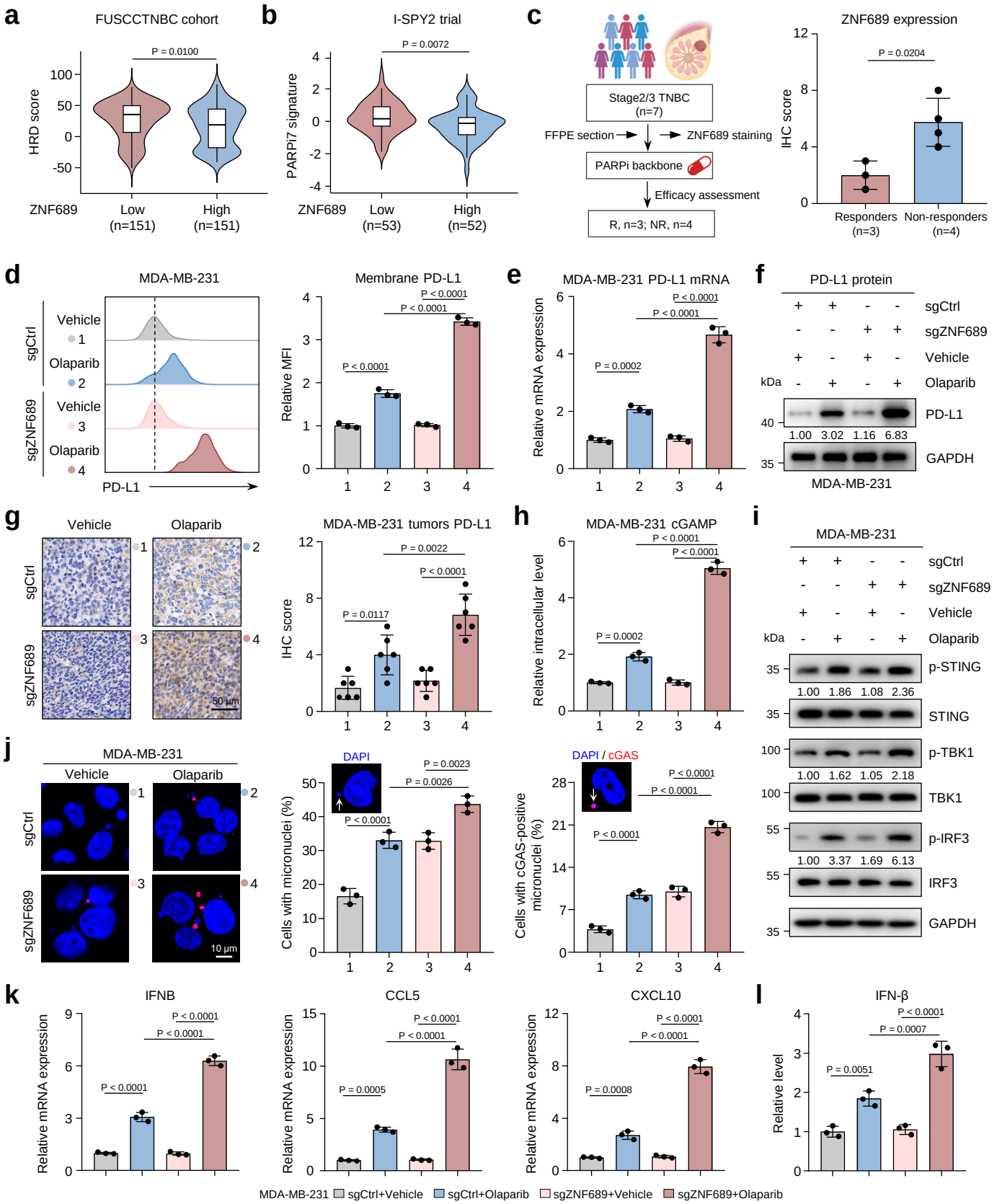
a
FUSCCTNBC cohort
P = 0.0100
HRD score
ZNF689
Low (n=151)
High (n=151)
b
I-SPY2 trial
P = 0.0072
PARPi7 signature
ZNF689
Low (n=53)
High (n=52)
c
Stage2/3 TNBC (n=7)
FFPE section
ZNF689 staining
PARPi backbone
Efficacy assessment
R, n=3; NR, n=4
ZNF689 expression
P = 0.0204
IHC score
Responders (n=3)
Non-responders (n=4)
d
MDA-MB-231
sgCtrl
Vehicle
Olaparib
sgZNF689
PD-L1
Membrane PD-L1
Relative MFI
e
MDA-MB-231 PD-L1 mRNA
Relative mRNA expression
P = 0.0002
f
PD-L1 protein
sgCtrl
sgZNF689
Vehicle
Olaparib
kDa
PD-L1
GAPDH
1.00 3.02 1.16 6.83
MDA-MB-231
g
Vehicle
Olaparib
sgCtrl
sgZNF689
50 μm
MDA-MB-231 tumors PD-L1
IHC score
P = 0.0022
P = 0.0117
h
MDA-MB-231 cGAMP
Relative intracellular level
P = 0.0002
i
MDA-MB-231
sgCtrl
sgZNF689
Vehicle
Olaparib
kDa
p-STING
STING
p-TBK1
TBK1
p-IRF3
IRF3
GAPDH
1.00 1.86 1.08 2.36
1.00 1.62 1.05 2.18
1.00 3.37 1.69 6.13
j
MDA-MB-231
Vehicle
Olaparib
sgCtrl
sgZNF689
10 μm
DAPI
Cells with micronuclei (%)
P = 0.0023
P = 0.0026
DAPI / cGAS
Cells with cGAS-positive micronuclei (%)
k
IFNB
CCL5
CXCL10
Relative mRNA expression
P = 0.0005
P = 0.0008
l
IFN-β
Relative level
P = 0.0051
P = 0.0007
MDA-MB-231 sgCtrl+Vehicle sgCtrl+Olaparib sgZNF689+Vehicle sgZNF689+Olaparib

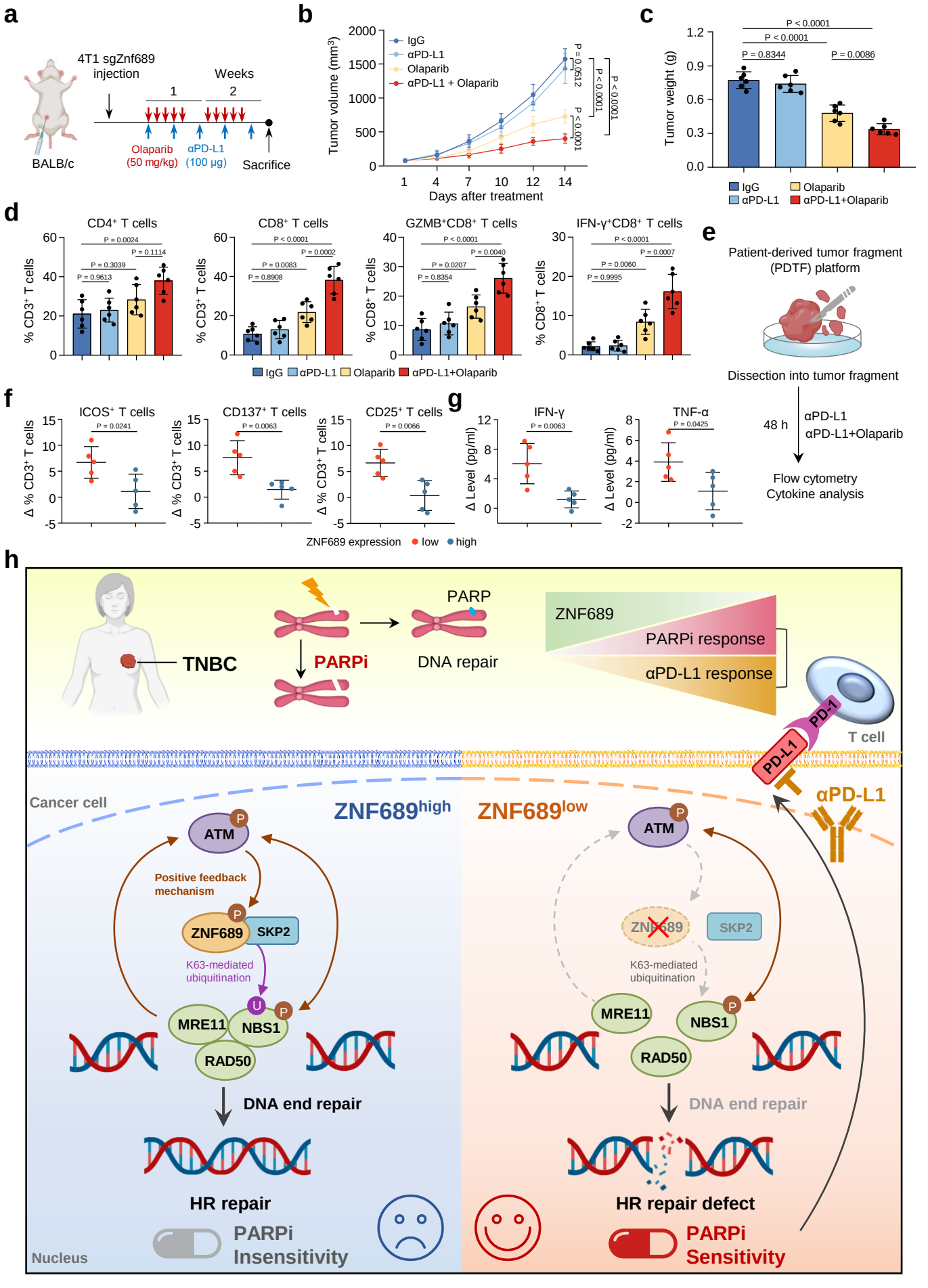
a
4T1 sgZnf689 injection
Weeks
1
2
BALB/c
Olaparib (50 mg/kg)
αPD-L1 (100 μg)
Sacrifice
b
Tumor volume (mm³)
IgG
αPD-L1
Olaparib
αPD-L1 + Olaparib
Days after treatment
c
Tumor weight (g)
P = 0.8344
P = 0.0086
IgG
αPD-L1
Olaparib
αPD-L1+Olaparib
d
CD4⁺ T cells
CD8⁺ T cells
GZMB⁺CD8⁺ T cells
IFN-γ⁺CD8⁺ T cells
% CD3⁺ T cells
% CD8⁺ T cells
e
Patient-derived tumor fragment (PDTF) platform
Dissection into tumor fragment
48 h
αPD-L1
αPD-L1+Olaparib
Flow cytometry
Cytokine analysis
f
ICOS⁺ T cells
CD137⁺ T cells
CD25⁺ T cells
Δ % CD3⁺ T cells
g
IFN-γ
TNF-α
Δ Level (pg/ml)
ZNF689 expression low high
h
TNBC
PARPi
PARP
DNA repair
ZNF689
PARPi response
αPD-L1 response
PD-1
PD-L1
T cell
αPD-L1
Cancer cell
ZNF689high
ZNF689low
ATM
Positive feedback mechanism
ZNF689
SKP2
K63-mediated ubiquitination
MRE11
NBS1
RAD50
DNA end repair
HR repair
PARPi Insensitivity
HR repair defect
PARPi Sensitivity
Nucleus